Identification and Control of a 3-X Cable-Driven Manipulator Inspired From the Bird's Neck

Benjamin Fasquelle, Parag Khanna, Christine Chevallereau, Damien Chablat, Denis Creusot, Stéphane Jolivet, Philippe Lemoine, Philippe Wenger

▶ To cite this version:

Benjamin Fasquelle, Parag Khanna, Christine Chevallereau, Damien Chablat, Denis Creusot, et al.. Identification and Control of a 3-X Cable-Driven Manipulator Inspired From the Bird's Neck. Journal of Mechanisms and Robotics, American Society of Mechanical Engineers, 2022, 14 (1), 10.1115/1.4051521 . hal-03314549

Identification and control of a 3-X cable-driven manipulator inspired from the bird neck

Benjamin Fasquelle, Parag Khanna, Christine Chevallereau, Damien Chablat,
Denis Creusot, Stéphane Jolivet, Philippe Lemoine
Ecole Centrale de Nantes, Centre National de la Recherche Scientifique,
Laboratoire des Sciences du Numérique de Nantes (LS2N)
UMR CNRS 6004, 1 rue de la Noë, 44321 Nantes
France

Philippe Wenger*
CNRS,
Laboratoire des Sciences du Numérique de Nantes (LS2N)
UMR CNRS 6004, 1 rue de la Noë,
44321 Nantes
France
Email: Philippe.Wenger@ls2n.fr

ABSTRACT

This paper is devoted to the control and identification of a manipulator with three anti-parallelogram joints in series, referred to as X-joints. Each X-joint is a tensegrity one-degree-of-freedom mechanism antagonistically actuated with cables and springs in parallel. As compared to manipulators built with simple revolute joints in series, manipulators with tensegrity X-joint offer a number of advantages, such as an intrinsic stability, variable stiffness and lower inertia. This design was inspired by the musculosleketon architecture of the bird neck, which is known to be very dextrous. A test-bed prototype is presented and used to test computed torque control laws. Friction and cable elasticity are modelled and identified. Their effect on the performance of control laws is analyzed. It is shown that in the context of antagonistic actuation and light weight design, friction plays a leading role and the significance of modelling cable elasticity is discussed.

Nomenclature

b	Base bar length
L	Diagonal bar length
$\psi = [\psi_1, \psi_2, \psi_3]^T$	Vector of angles between the base bar and a diagonal bar of the X-joints
r	pulley radius
r_d	drum radius
R	gear ratio
I_a	motor inertia
$\theta = [\theta_1, \theta_2, \theta_3, \theta_4]^T$	Vector of motor angular positions measured at the motor shaft
θ^d	Vector of motor angular positions corresponding to the desired trajectory
$\mathbf{f} = [f_1, f_2, f_3, f_4]^T$	Vector of input forces
$\alpha = [\alpha_1, \alpha_2, \alpha_3]^T$	Vector of X-joint orientation angles
$\hat{\alpha}$	Vector of estimation of X-joint orientation
α_{IP}	Vector of X-joint orientation angles obtained from video and image processing
α_d	Vector of X-joint desired orientation angles
$\mathbf{l}_c = [l_{c1}, l_{c2}, l_{c3}, l_{c4}]^T$	Vector of cable variable lengths
$\mathbf{x}_c = [x_{c1}, x_{c2}, x_{c3}, x_{c4}]^T$	Vector of cable elongations

$\mathbf{t}_c = [t_{c1}, t_{c2}, t_{c3}, t_{c4}]^T$	Vector of cable tensions
$\mathbf{k} = [k(1), k(2), k(3), k(4)]^T$	Vector of cable stiffnesses
$\mathbf{c}_a = [c_a(1), c_a(2), c_a(3), c_a(4)]^T$	Vector of cable damping
$\lambda = [\lambda(1), \lambda(2), \lambda(3), \lambda(4)]^T$	Vector of variable stiffness coefficients
$\mathbf{f}_{friction}$	Friction model
$\mathbf{f}_s = [f_s(1), f_s(2), f_s(3), f_s(4)]^T$	Vector of friction coefficients
c_s	Coefficient used to adjust friction at stop
$\mathbf{Z}$	Cable transmission matrix of size 3×4
$\mathbf{M}$	Inertia matrix of the whole manipulator (including geared motors)
$\mathbf{M_m}$	Inertia matrix of the manipulator (without geared motors)
$\mathbf{c}$	Vector of Coriolis effects affecting the manipulator and geared motors
$\mathbf{c_m}$	Vector of Coriolis effects affecting the manipulator (without geared motors)
$\mathbf{g}$	Gradient of the manipulator potential energy
$\mathbf{v}$	Vector of parameters to identify
$\mathbf{W}$	Observation matrix
$\mathbf{C}_x$	Covariance matrix
σ_i	Standard deviation of parameter i
ρ	Vector of residues
$k_i = \omega^3, k_v = 3\omega, k_p = 3\omega^2$	Gains of the PID control
Γ^d	Vector of desired torques
t_{min}	Minimal tension in cables
f_{min}	Minimal actuation force

1 Introduction

Bio-inspired design has drawn the interest of many researchers and is an interesting avenue for designing light-weight manipulators. Such manipulators are desired in a number of applications, in particular when safe interactions or high dynamics are required. Cable-driven manipulators, which mimick the muscles-and-tendons actuation system met in animals, are good candidates for light weight design, since the motors can be fixed on the ground. Two main families are considered in the literature, namely, continuum manipulators and discrete manipulators. Inspired from the elephant trunk or the octopus tentacle, the former have a flexible structure and, consequently, infinitely many degrees of freedom. They find applications in highly cluttered environments and their accurate modeling is a real challenge [1]. The latter consist of a discrete number of joints, as in the musculoskeletal system of vertebrates. They can be more easily modelled and are still interesting solutions for designing dextrous manipulators [2, 3]. Applications include environmentally interactive robots [4], robotic hands [5], exoskeletons [6], and other medical devices [7].

The general frame of this work is the design and control of a robotic manipulator inspired by the bird neck. Birds use their neck like an arm for every-day-life tasks. Cleaning and feeding necessitates dexterity while high force transmission and accelerations are required when a woodpecker hits a tree trunk. We have built a preliminary manipulator model to mimick the neck of a woodpecker, which moves mainly in a vertical plane [8, 9]. Bird necks have a variable number of vertebrae, ranging from 10 in parrots to 26 in swans [10]. This preliminary model uses three joints. This choice was not only motivated to start with a simple design: from a biological point of view, indeed, the bird neck can be regarded as a serial assembly of three main sets of vertebrae, each set having its own function [10]. The prototype consists of the serial assembly of three tensegrity joints remotely actuated with cables. A tensegrity structure is an assembly of compressive elements (bars) and tensile elements (cables, springs) held together in equilibrium [11, 12]. Tensegrity is known in architecture and art for more than a century [13] and is suitable for aerospace applications [14, 15] and for modeling living organisms [16]. Tensegrity mechanisms have been more recently studied for their promising properties in robotics such as low inertia, natural compliance and deployability [17,18,19]. The tensegrity joints used in our neck model are anti-parallelogram joints inspired from the Snelson's X-shape mechanisms [20], referred to as *X-joints* in this paper. As compared with simple revolute joints, X-joints do not have a fixed rotation axis, a common feature in biological joints [21, 9]. Moreover, they have a number of advantages such as larger rotation ranges [4] and larger variations of stiffness [22].

Cable-driven manipulators raise a number of difficulties, such as the choice of suitable routing strategies [3, 23, 2] and accounting for cable flexibility [24, 25, 26]. Moreover, the control of cable-driven manipulators is also a challenging task [27, 28]. In [7], a control strategy to compensate friction was proposed but it relied on a measurement of cable tension, which adds complexity and is not available in our prototype. In other papers such as in [29], force sensors are used for the identification and a compensation of the identified model is then integrated by control. In the proposed paper, the cable driven robot used is not a cable-driven parallel robot such as in [26], nor a tendon-based actuation system with tendons sliding in curved pathways such as in [29]. Accordingly, the effects of cable elongation modelling differ. Moreover, our identification method and control strategy do not use any tension sensors. This paper is devoted to the identification and control of a 3-X

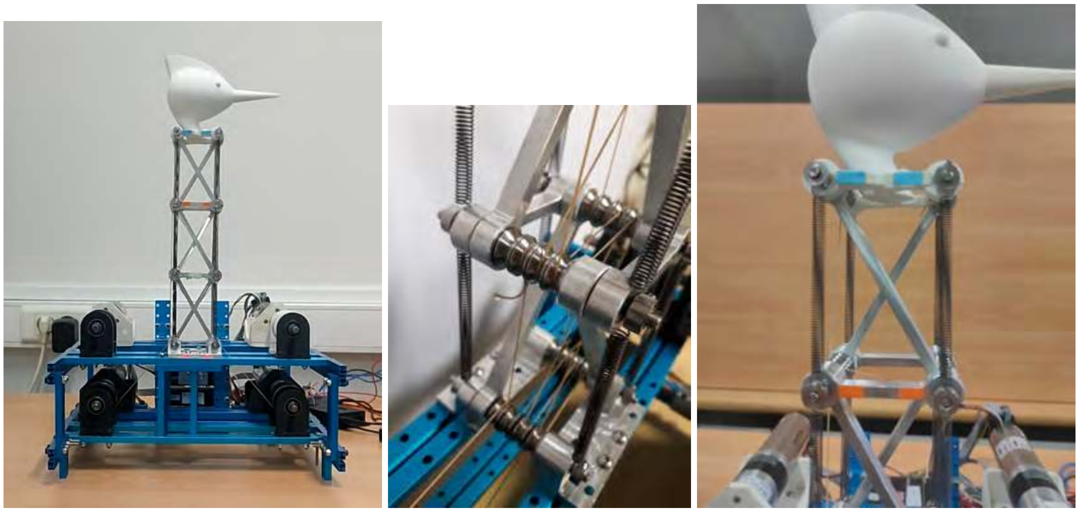

Fig. 1: Left: our prototype with its three X-joints and four motors. Center: pulley arrangement. Right: coloured markers on base and top bars of the third mechanism.

manipulator remotely actuated with cables. Two main sets of parameters are identified: geared motor frictions and cable stiffnesses. The identification has a variety of objectives such as: to better understand our system, to build a simulator that is closer to the experiments or to test several control strategies. Periodic identification campaigns can also be conducted for the purpose of monitoring cable wear. Model-based control laws, which use the dynamic model of the complete system, are implemented and tested on a testbed prototype. We want to explore the impact of the identified friction and cable stiffness models on the performance of control law.

Next section describes the experimental set-up. Section 3 presents the cable transmission and dynamic models. Calculation of the manipulator joint configuration from the actuator encoders is presented in section 4. Friction and cable elongation models as well as their associated identification models are discussed in section 5. Section 6 proposes computed torque control laws and test results are discussed in section 7. Last section concludes this paper.

2 Experimental set-up

2.1 Manipulator architecture

The experimental set up is a series assembly of 3 cable-driven X-joints. Each joint is equipped with two lateral springs of equal stiffness and assumed mass-less (figure 1). Springs have been often used in tensegrity mechanisms [17, 18, 19]. The role of springs is to assure a minimal stiffness. Spring stiffnesses used in our prototype were chosen to have a stable equilibrium at rest and their rest length l_0 was chosen so that the springs remain always in tension. Finally, we came up with a set of commercial springs with the following features: two springs of stiffness $300N.m^{-1}$ arranged in parallel on each side of the first X-joint (defining an equivalent $600N.m^{-1}$ stiffness spring on each side) and one spring of stiffness $200N.m^{-1}$ on each side of the second and third X-joint; rest length $l_0 = 0.046$ for all springs.

To avoid self collisions, the crossing bars have been assembled in two parallel planes and the top and base bars are present in each plane. This arrangement also reduces deformation out of the vertical plane. In the original Snelson X-shape mechanism, the top and bottom sides are cables or springs. Here, only one degree of freedom is desired. To avoid any undesired rotation of the diagonal bars, the top and bottom cables have been replaced with rigid bars. The resulting mechanism is still a tensegrity one, but it is of class 2 (for the first and third joint) and 3 (for the second joint), instead of class 1 [13]. The top bar of the first joint (resp. second joint) is the same as the bottom bar of the second joint (resp. third joint). The configuration of each joint i is defined by the orientation angle α_i of its top bar with respect to its base bar. All revolute joints connecting the links are assumed perfect. The two diagonal bars have the same length ($L = 100mm$) while the top and base bars have the same length $b = 50mm$.

2.2 Actuation

The three joints are driven remotely with cables controlled by winches mounted on rotary motors. Ball bearing-mounted loose pulleys are used to guide the cables from the winches to the X-joints. All pulleys are mounted on the axes linking the rigid bars and arranged in four rows. Thus, each cable has its own row and does not cross each other, as shown in Fig. 1. The number of active cables needs to be determined properly. We want to control the orientation angle of the three X-joints. In theory, a minimum of three active cables is required. In practise, at least one more cable is required to produce a

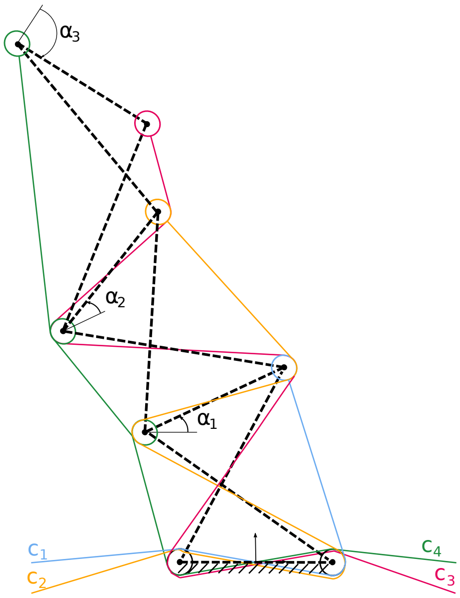

Fig. 2: Actuation scheme of the 3-X cable driven manipulator prototype.

sufficiently large wrench-feasible workspace [30, 23]. The maximum number is six, a scheme where each X-joint would be antagonistically actuated with two cables, one on each side. We propose to use four motors. This choice is a compromise that allows controlling the three joints with a reasonable number of motors. Several cable routing strategies can be considered, including strut-routed (i.e. passing along rigid bars [31]) and side-routed (i.e. running on sides through springs [4], [23]). We propose to use a hybrid strut-routed/side-routed strategy. One long cable is run in a side-routed way through the left sides of the three X-joints and is attached to the last X-joint (see Fig. 2). This cable (shown in green) actuates the three X-joints simultaneously. On the right sides, three cables are run through the X-joints and attached to the right tip of the top bar of the driven X-joint. If there were no pulleys, each of those three cables would move solely one X-joint. As it will be shown in next section, however, the presence of pulleys induces slight couplings. In the woodpecker neck, the long, left side-routed cable corresponds to a powerful muscle found all along the front of the neck. This muscle allows the neck to quickly propel its head to hit tree trunks [8]. The other cables correspond to other muscles present to adjust the movements. The path of each cable has been adjusted to avoid any loss of contact between pulleys and cables. In particular, the green cable wraps around the two intermediate pulleys by making at least one turn. Each cable is attached to a drum linked to a motor shaft. The first motor pulls the side-routed green cable, which wraps around the two left-sided intermediate pulleys to ensure contact. Each of the other three motors pulls one X-joint on its right. The yellow and red cables that drive the second and third joint, respectively, are strut routed. All pulleys have a radius of $r = 4.6mm$ and the four drums have a radius of $r_d = 20mm$. The four motors are MAXON brushless gearmotors (ECMAX40L/PM42) with a gear ratio of $R = 25$. Four ESCON 50/5 controllers ensures velocity and torque control of the motors. The frequency of the control law is $500Hz$. The motors interact with a Beaglebone (BB) blue microcontroller, on which the control law is programmed.

3 Cable length and dynamic models

This section is devoted to the derivation of the cable length and dynamic models of the manipulator. The input variables of our system are the forces applied by the motors on the cables. Our goal is to control the orientation angles α_i of each X-joint. The X-joints are numbered from bottom to top. Since the only measured variables are the motor angular positions θ_i, α_i must be computed from θ_i. To this end, the relationship between the cable lengths and the orientation angles of the X-joints is first established.

3.1 Cable length model

Pulleys used to guide the cables from the winches to the X-joints affect the calculation of the unrolled cable lengths required for desired orientation angles α_i by adding some coupling between the X-joints. In [9], a simplified cable length model was used by neglecting the radii of all pulleys, which induced some errors in the model. We now derive the expression of each unrolled cable length as a function of the orientation angle α_i by taking into account the pulleys properly.

Let $l_l(\alpha_i)$ and $l_r(\alpha_i)$ be the left and right side lengths of each X-joint, respectively, which correspond to the spring

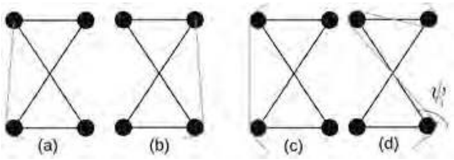

Fig. 3: The four cases met for cable variable lengths calculation, referred to as (a)-(d) from left to right. The variable part of the cable length as a function of α_i is defined by Eq. (3) to (6) for cases (a) to (d), respectively.

lengths. Their expression is [23]:

$$l_l(\alpha_i) = \sqrt{L^2 - b^2\cos^2(\frac{\alpha_i}{2})} - b\sin(\frac{\alpha_i}{2}) \tag{1}$$

$$l_r(\alpha_i) = \sqrt{L^2 - b^2\cos^2(\frac{\alpha_i}{2})} + b\sin(\frac{\alpha_i}{2}). \tag{2}$$

The unrolled length of each cable can be expressed as the sum of a variable length that depends on α_i and on a constant length that needs not be determined. The variable length calculation depends on the cable way along each X-joint. Pulleys used to guide cables must be taken into account and add some complexity in the calculations. A kinematic model of the cables considering pulleys was derived in [32] for a cable-driven parallel manipulator. For the manipulator at hand, four different cases must be considered, as shown in Fig. 3. For the first two cases shown on the left of Fig. 3, referred to as (a) and (b), the left and right variable length $l_i(\alpha_i)$ can be written as, respectively (see [33] for more details):

$$l_i(\alpha_i) = \sqrt{l_l(\alpha_i)^2 - r^2} + r\Big(-\arctan(\frac{\sqrt{l_l(\alpha_i)^2 - r^2}}{r}) - \frac{\alpha_i}{2}\Big) \tag{3}$$

$$l_i(\alpha_i) = \sqrt{l_r(\alpha_i)^2 - r^2} + r\Big(\frac{\alpha_i}{2} - \arctan(\frac{\sqrt{l_r(\alpha_i)^2 - r^2}}{r})\Big). \tag{4}$$

For the third case, referred to as (c) in Fig. 3, the variable length is [33]:

$$l_i(\alpha_i) = l_l(\alpha_i) - r\alpha_i. \tag{5}$$

Finally, the variable length associated with the fourth case (Figure 3, right), referred to as (d), corresponds to the strut routing scheme and can be expressed as [33]:

$$l_i(\alpha_i) = r(2\psi(\alpha_i) - \alpha_i), \tag{6}$$

where $\psi(\alpha_i)$ is the angle between the diagonal bar and the base bar as shown in Fig. 3, right. It can be expressed as follows [34]:

$$\psi_i = 2\arctan\Big(\frac{-2L\sin(\alpha_i) - \sqrt{(2L\sin(\alpha_i))^2 + (2l(\cos(\alpha_i)+1))^2 - (2b(\cos(\alpha_i)+1))^2}}{(2b-2L)(\cos(\alpha_i)+1)}\Big). \tag{7}$$

To obtain the total variable length associated with each cable, the appropriate cable case (a), (b), (c) or (d) along each X-joint must be first identified. Then, the associated variable lengths must be added together.

The blue cable c_1 is attached to the first X-joint (Figure 2) and its way simply follows case (b) along this sole joint. Thus, its variable length l_{c1} can be directly computed from Eq. (3) by:

$$l_{c1} = \sqrt{l_l(\alpha_1)^2 - r^2} + r\Big(\frac{\alpha_1}{2} - \arctan(\frac{\sqrt{l_l(\alpha_1)^2 - r^2}}{r})\Big). \tag{8}$$

The yellow cable c_2 is attached to the second X-joint (see Fig. 2) and follows a way corresponding to case (d) along the first X-joint (Figure 3, right), and to case (b) along the second X-joint (Figure 3, left). Its variable length l_{c2} can thus be written as:

$$l_{c2} = \sum_{i=1}^{2} l_i(\alpha_i), \tag{9}$$

with:

$$l_1(\alpha_1) = r(2\psi_1 - \alpha_1) \tag{10}$$

$$l_2(\alpha_2) = \sqrt{l_r(\alpha_2)^2 - r^2} + r\Big(\frac{\alpha_2}{2} - \arctan(\frac{\sqrt{l_r(\alpha_2)^2 - r^2}}{r})\Big). \tag{11}$$

The red cable c_3 follows a way similar to the yellow cable, with the difference that it has to go up to the third X-joint (see Fig. 2). Its variable length l_{c3} can be written as:

$$l_{c3} = \sum_{i=1}^{3} l_i(\alpha_i), \tag{12}$$

where:

$$l_1(\alpha_1) = r(2\psi_1 - \alpha_1) \tag{13}$$

$$l_2(\alpha_2) = r(2\psi_2 - \alpha_2) \tag{14}$$

$$l_3(\alpha_3) = \sqrt{l_r(\alpha_3)^2 - r^2} + r\Big(\frac{\alpha_3}{2} - \arctan(\frac{\sqrt{l_r(\alpha_3)^2 - r^2}}{r})\Big). \tag{15}$$

Finally, the green cable running along the left side of the manipulator, referred to as c_4 (see Fig. 2) is attached to the last X-joint and follows a way corresponding to case (c) along the first two X-joints (Figure 3, middle) and to case (a) along the last X-joint (Figure 3, left). Accordingly, the variable length l_{c4} of this cable can be written as:

$$l_{c4} = \sum_{i=1}^{3} l_i(\alpha_i), \tag{16}$$

where:

$$l_1(\alpha_1) = l_l(\alpha_1) - r\alpha_1 \tag{17}$$

$$l_2(\alpha_2) = l_l(\alpha_2) - r\alpha_2 \tag{18}$$

$$l_3(\alpha_3) = \sqrt{l_l(\alpha_3)^2 - r^2} + r\Big(\arctan(-\frac{\sqrt{l_l(\alpha_3)^2 - r^2}}{r}) - \frac{\alpha_3}{2}\Big). \tag{19}$$

Let us set $\theta_i = 0,\ i = 1,..,4$ and $\mathbf{l}_c = \mathbf{l}_{c0}$ when $\alpha_i = 0, i = 1,..3$ (the manipulator is at rest, i.e., straight right).

Assuming inextensible cables, the motor positions can be expressed as functions of the cable lengths by the following vector equation:

$$\theta = -\frac{R}{r_d}(\mathbf{l}_c - \mathbf{l}_{c0}), \tag{20}$$

where $\theta = [\theta_1, \theta_2, \theta_3, \theta_4]^T$, $\mathbf{l}_c = [l_{c1}, l_{c2}, l_{c3}, l_{c4}]^T$ and $\mathbf{l}_{c0}$ is the value of $\mathbf{l}_c$ at rest. We assume that $\theta_i > 0$ when motor i winds up cable c_i, hence the minus sign in the above expression. As a reminder, r_d is the drum radius and R is the reduction ratio.

As a result, the motor velocities $\dot{\theta}$ can be expressed as functions of the X-joint velocities $\dot{\alpha}$ as:

$$\dot{\theta} = \frac{R}{r_d}\mathbf{Z}^T(\alpha)\dot{\alpha}, \tag{21}$$

where $\mathbf{Z}$ is the cable transmission 3×4 matrix, whose elements are Z_{ij}:

$$\mathbf{Z}_{ij} = -\frac{\partial l_c(j)}{\partial \alpha_i}. \tag{22}$$

This matrix can be decomposed into the form:

$$\mathbf{Z} = (\mathbf{Z}_1\ \mathbf{Z}_2), \tag{23}$$

where $\mathbf{Z}_1$ is a 3×3 triangular matrix associated with the blue, yellow and red cables pulling on the right, and $\mathbf{Z}_2$ is a vector of size 3 associated with the green cable pulling on the left. Thus, the diagonal entries of $\mathbf{Z}_1$ are of constant sign opposite to the sign of the components of $\mathbf{Z}_2$ and $\mathbf{Z}_1$ is invertible. Moreover, the non-diagonal entries of $\mathbf{Z}_1$, which are due to the pulleys, are small as compared to the diagonal entries because the pulleys' radii are small as compared to the X-joint size. This decomposition will be used in section 6 for control.

3.2 Dynamic model

Let $\mathbf{M}$ be the inertia matrix accounting for the manipulator inertia $\mathbf{M}_m$ [35] and for the geared motors inertia:

$$\mathbf{M}(\alpha) = \mathbf{M}_m(\alpha) + I_a\left(\frac{R}{r_d}\right)^2 \mathbf{Z}(\alpha)\mathbf{Z}(\alpha)^T, \tag{24}$$

where I_a is the inertia of the geared motors. The inertia matrix $\mathbf{M}(\alpha)$ is deduced from the kinetic energy. All geared motors are identical and their total contribution to the kinetic energy is $\frac{I_a}{2}\dot{\theta}^T\dot{\theta}$. It can also be written $\frac{I_a}{2}\left(\frac{R}{r_d}\right)^2 \dot{\alpha}^T\mathbf{Z}(\alpha)\mathbf{Z}(\alpha)^T\dot{\alpha}$ using the relationship between motors and X-joints rotation angles given in Eq. (21). Neglecting friction and cable elasticity, a first dynamic model can be derived as follows [9]:

$$\mathbf{M}(\alpha)\ddot{\alpha} + \mathbf{c}(\alpha, \dot{\alpha}) + \mathbf{g}(\alpha) = \mathbf{Z}(\alpha)\mathbf{f}, \tag{25}$$

where $\mathbf{g}$ is the gradient of the manipulator potential energy with respect to the generalized coordinates, its includes the gravity and spring forces, $\mathbf{f} = [f_1, f_2, f_3, f_4]^T$ is the vector of motor forces transmitted by the cables and $\mathbf{c}$ is the vector of Coriolis effects affecting the manipulator, $\mathbf{c}_m$, and the geared motors:

$$\mathbf{c} = \mathbf{c}_m(\alpha) + I_a\left(\frac{R}{r_d}\right)^2 \dot{\mathbf{Z}}(\alpha, \dot{\alpha})\mathbf{Z}(\alpha)^T. \tag{26}$$

where the second term of LHS (left-hand-side) of equation (26) comes from the contributions of the geared motors to the kinetic energy. The control law tested in [9] was based on this dynamic model but the cable transmission matrix $\mathbf{Z}$ was calculated by neglecting the effects of pulleys. With this control law, large oscillations in the applied forces were observed and values of α computed by the control were significantly different from the observed ones. In order to obtain a better control, an improved dynamic model is proposed thereafter, including pulley effects, motor friction and cable elasticity. Friction and cable elasticity must be identified. All other parameters appearing in the dynamic model are available from the CAD model of our prototype and from motor data-sheets. Since the manipulator is intrinsically light and because of the reduction gear, the contribution of $\mathbf{M}_m$ in Eq. (24) is low as compared to the contribution inertia of the geared motors. On the other hand, this latter cannot be assumed constant as it is generally the case in manipulators that are not driven with cables. Indeed, matrix $\mathbf{Z}$ depends on the cable routing and on α. The inertia matrix $\mathbf{M}$ is therefore variable and it is important to take it into account in our models and in the control.

3.3 Dynamic model with friction and elastic cables

All cables are now considered elastic. Assuming $\theta_i = 0,\ i = 1,..,4$ when $\alpha_i = 0, i = 1,..3$ at rest (i.e. with zero forces applied and, thus, with zero cable elongations), the vector of cable elastic elongations $\mathbf{x}_c = [x_{c1}, x_{c2}, x_{c3}, x_{c4}]^T$ is defined as:

$$\mathbf{x}_c = \mathbf{l}_c - \mathbf{l}_{c0} - \frac{r_d}{R}\theta. \tag{27}$$

In other words, the elongation of each cable is defined as the difference between its theoretical length as calculated in section 3.1 and the cable length wrapped around the associated winch.

Upon differentiating Eq. (27) with respect to time, we obtain:

$$\mathbf{Z}(\alpha)^T\dot{\alpha} = \frac{r_d}{R}\dot{\theta} + \dot{\mathbf{x}}_c. \tag{28}$$

Let $\mathbf{t}_c = [t_{c1}, t_{c2}, t_{c3}, t_{c4}]^T$ define the vector of cable tensions and let $\mathbf{f}_{friction}$ be the vector of friction forces. Friction mostly occurs in the geared motors. Modelling friction in pulleys can be of interest to improve measurement accuracy of cable force sensors [36]. In this paper, no cable force sensors are used. We thus concentrate on modelling friction due the geared motors. Writing the dynamic model for the system made of the geared motors and of the cables, provides the following motion equation of θ:

$$I_a\ddot{\theta} + \frac{r_d}{R}\mathbf{t}_c + \frac{r_d}{R}\mathbf{f}_{friction} = \frac{r_d}{R}\mathbf{f}. \tag{29}$$

The dynamic model written for the manipulator and the cables gives the motion equation of α:

$$\mathbf{M}_m(\alpha)\ddot{\alpha} + \mathbf{c}_m(\alpha,\dot{\alpha}) + \mathbf{g}(\alpha) = \mathbf{Z}(\alpha)\mathbf{t}_c. \tag{30}$$

Upon differentiating Eq. (28) with respect to time and substituting $\ddot{\theta}$ into Eq. (29), cable tension can be expressed as follows:

$$\mathbf{t}_c = \mathbf{f} - \mathbf{f}_{friction} - I_a(\frac{R}{r_d})^2(\mathbf{Z}(\alpha)^T\ddot{\alpha} + \dot{\mathbf{Z}}(\alpha)^T\dot{\alpha} - \ddot{\mathbf{x}}_c). \tag{31}$$

Substituting the above expression into Eq. (30) gives the dynamic model of the full system with friction and cable elasticity:

$$\mathbf{M}(\alpha)\ddot{\alpha} + \mathbf{c}(\alpha,\dot{\alpha}) + \mathbf{g}(\alpha) = \mathbf{Z}(\alpha)\Big(\mathbf{f} - \mathbf{f}_{friction} + I_a(\frac{R}{r_d})^2\ddot{\mathbf{x}}_c\Big). \tag{32}$$

Friction and cable elasticity must be then identified.

4 Estimation of α : $\hat{\alpha}$

Our prototype is not equipped with encoders to measure α online. $\hat{\alpha}$ can be reconstructed from θ (measured by the motor encoders) through cable lengths with the cable models derived in section 3.1. On the other hand, cable elasticity must be taken into account. Consequently, cable stiffness must be identified. To this end, the elongation of the cables are calculated from external measurements of α using video recording during the identification experiments.

4.1 Calculation of $\hat{\alpha}$ from θ

Two methods are considered to compute $\hat{\alpha}$ from the measured values of θ. We assume in this section that the cable elongation $\mathbf{x}_c$ and its derivative are known from the identified cable stiffness and from the cable tensions. The proposed methods can be also used with inelastic cables by setting $\mathbf{x}_c = 0$.

In the first method, the minimal number of measurement data of θ, namely, 3, is used. The estimation $\hat{\alpha}$ then relies on the model of cable elasticity and this method can be used to evaluate the quality of this model.

The second method uses all the 4 available measurement data of θ. The estimation $\hat{\alpha}$ is defined as a compromise between these 4 information data. Accordingly, the estimation reliability is less dependent on the quality of the model of cable elasticity.

4.1.1 Calculation from three components of θ

The first method uses only 3 components of θ. The idea is to calculate the X-joint orientations $\hat{\alpha}_1$, $\hat{\alpha}_2$ and $\hat{\alpha}_3$ recursively as functions of the lengths of right cables (i.e. the blue, yellow and red cables used to actuate the first, second and third X-joint). The X-joint orientation $\hat{\alpha}_1$ is first computed from the length l_{c1} of the blue cable (Figure 2) using Eqs. (8) and (27). Knowing $\hat{\alpha}_1$, $\hat{\alpha}_2$ is then computed from the length l_{c2} of the yellow cable using Eqs. (9) and (27).

Knowing $\hat{\alpha}_1$ and $\hat{\alpha}_2$, $\hat{\alpha}_3$ is finally computed from the length l_{c3} of the red cable with Eqs. (12) and (27). The following triangular system is obtained:

$$\begin{cases} \hat{\alpha}_1 = f^1(\theta_1, x_{c1}) \\ \hat{\alpha}_2 = f^2(\theta_1, \theta_2, x_{c1}, x_{c2}) \\ \hat{\alpha}_3 = f^3(\theta_1, \theta_2, \theta_3, x_{c1}, x_{c2}, x_{c3}). \end{cases} \tag{33}$$

No closed-form expressions could be found for this system. However, owing to the monotony of the cable length functions used to obtain the above system, we know that $\hat{\alpha}_1$, $\hat{\alpha}_2$ and $\hat{\alpha}_3$ are defined uniquely. We have implemented a simple, fast procedure to obtain approximated values of $\hat{\alpha}_i$ by linear interpolation from a pre-calculated set of solutions. The number of pre-calculated solutions is sufficiently large so that the error of $\hat{\alpha}_i$ is always lower than the resolution of the motor encoders.

4.1.2 Calculation from all components of θ

The second method to obtain $\hat{\alpha}$ from θ uses all components of θ. Knowing that the cables are elastic, the idea is to use all the measurements to have a more realistic computation.

Eq. (28) can be rewritten as:

$$\mathbf{Z}(\hat{\alpha}(t))^T \Big(\hat{\alpha}(t+\Delta t) - \hat{\alpha}(t)\Big) = \frac{r_d}{R}\Big(\theta(t+\Delta t) - \theta(t)\Big) + \Big(\mathbf{x}_c(t+\Delta t) - \mathbf{x}_c(t)\Big), \tag{34}$$

where Δt is a sufficiently small time step. The Moore–Penrose pseudo-inverse $\mathbf{Z}^{T+}$ allows computing the variation in $\hat{\alpha}$ that minimizes the error. Accordingly, $\hat{\alpha}$ can be computed as follows:

$$\hat{\alpha}(t+\Delta t) = \hat{\alpha}(t) + \mathbf{Z}(\hat{\alpha}(t))^{T+}\left[\frac{r_d}{R}\Big(\theta(t+\Delta t) - \theta(t)\Big) + \Big(\mathbf{x}_c(t+\Delta t) - \mathbf{x}_c(t)\Big)\right]. \tag{35}$$

4.2 Measuring α with image processing : $\alpha_{\mathbf{IP}}$

Identification of cable stiffness required knowledge of cable elongation and, in turn, of both θ and α. The former is measured from the motor encoders and the latter is measured by video. We use a camera with an image size of $1280x720$ pixels and 30 frames per second. During experiments, X-joints displacements are recorded. To this end, several coloured markers are placed on top and base bars of the three X-joints (see Fig. 1). Then α_{IP} is computed offline with an image processing (IP) algorithm on the basis of the markers. The target area for the IP analysis is kept in the centre of video to avoid any distortion. The first and second derivatives of α_{IP} are computed numerically. Note that the low video frequency does not allow using α_{IP} for control purposes, but it can be used for the identification experiments. The precision of the image processing is about $1deg$. This precision is acceptable in view of the errors encountered during control (see section 6).

5 Identification of friction and cable stiffness parameters

5.1 Identification model

Friction and elastic cable models are established in this section. We then derive a system of equations linear in the parameters to identify. We use an identification method successfully applied in [37] and [38]. This method is detailed in [39].

5.1.1 Friction equations

As written previously, friction is assumed to occur mainly in the geared motors. A dry friction model can be written as follows:

$$\mathbf{f}_{friction}(\mathbf{f}_s,\dot{\theta}) = diag(sign(\dot{\theta}))\mathbf{f}_s, \tag{36}$$

where $\mathbf{f}_s = [f_s(1), f_s(2), f_s(3), f_s(4)]^T$ is a constant vector that must be identified, $diag(\mathbf{u})$ is a diagonal (4×4) matrix built with the components of $\mathbf{u}$ and $sign$ is the sign function. A model ensuring continuity can be derived as follows:

$$\mathbf{f}_{friction}(\mathbf{f}_s,\dot{\theta}) = diag(\frac{2}{\pi}\arctan(c_s\dot{\theta}))\mathbf{f}_s, \tag{37}$$

where c_s is a tuning parameter that allows adjusting the slope of the arc-tangent around 0. This parameter is fixed arbitrarily to $c_s = 0.5$. Factor $\frac{2}{\pi}$ ensures that $\mathbf{f}_{friction}$ tends towards $\mathbf{f}_s$ and $-\mathbf{f}_s$ when $\dot{\theta}$ has large positive and negative values, respectively.

Substituting $\mathbf{f}_{friction}$ into Eq. (32), we obtain:

$$\mathbf{Z}(\alpha)diag(\frac{2}{\pi}\arctan(c_s\dot{\theta}))\mathbf{f}_s = \mathbf{Z}(\alpha)(\mathbf{f}+I_a(\frac{R}{r_d})^2\ddot{\mathbf{x}}_c) - \mathbf{M}(\alpha)\ddot{\alpha} - \mathbf{c}(\alpha,\dot{\alpha}) - \mathbf{g}(\alpha). \tag{38}$$

We thus obtain a system of three equations that are linear in $\mathbf{f}_s$. Once α, θ, their derivatives and $\mathbf{f}$ are known, $\mathbf{f}_s$ can thus be identified. A model with viscous friction was tested but this model did not provide better results, confirming that dry friction is preponderant [33].

5.1.2 Cable stiffness equations

During the identification experiments, α is obtained from the image processing $\alpha = \alpha_{\mathbf{IP}}$ and θ is measured by the motor encoders. Cable elongation $\mathbf{x}_c$ can be computed with Eq. (27).

This calculation assumes that there is no cable elongation in the initial manipulator configuration $\alpha_i = 0, i = 1,..,3$. In practise, the cables need to be slightly in tension to avoid slack, but the elongation is small and can be neglected. The derivative $\dot{\mathbf{x}}_c$ of $\mathbf{x}_c$ is computed numerically.

Rather than resorting to an elastic Young modulus based model [40], we prefer to write a more general cable model that makes it possible to identify a set of parameters for each cable:

$$\mathbf{t}_{ci} = k(i)x_{ci} + c_a(i)\dot{x}_{ci}, \tag{39}$$

or, in vector form:

$$\mathbf{t}_c = diag(\mathbf{x}_c)\mathbf{k} + diag(\dot{\mathbf{x}}_c)\mathbf{c}_a, \tag{40}$$

where $\mathbf{k} = [k(1), k(2), k(3), k(4)]^T$ is the constant vector of cable stiffnesses and $\mathbf{c}_a = [c_a(1), c_a(2), c_a(3), c_a(4)]^T$ is the constant vector of damping coefficients. Using equation (29) and the friction model, the vector of cable tensions can be written as:

$$\mathbf{t}_c = \mathbf{f} - diag(\frac{2}{\pi}\arctan(c_s\dot{\boldsymbol{\theta}}))\mathbf{f}_s - \frac{R}{r_d}I_a\ddot{\boldsymbol{\theta}}. \tag{41}$$

Combining Eqs. (40) and (41), the following vector equation is obtained:

$$diag(\mathbf{x}_c)\mathbf{k} + diag(\dot{\mathbf{x}}_c)\mathbf{c}_a = \mathbf{f} - diag(\frac{2}{\pi}\arctan(c_s\dot{\boldsymbol{\theta}}))\mathbf{f}_s - \frac{R}{r_d}I_a\ddot{\boldsymbol{\theta}}. \tag{42}$$

This vector equation provides four equations that are linear in the friction, stiffness and damping coefficients of each cable.

5.1.3 Complete linear system

Eqs. (38) and (42), which describe the contribution of friction in the dynamic model and in the cable stiffness model, respectively, are now gathered to obtain a system of equations linear in the parameters to identify:

$$\mathbf{D}\mathbf{v} = \mathbf{y}, \tag{43}$$

where $\mathbf{v}$ if the vector of $n_p = 12$ parameters to identify: $\mathbf{v} = \begin{pmatrix}\mathbf{k} & \mathbf{c}_a & \mathbf{f}_s\end{pmatrix}^T$. Now, the contribution of friction in Eqs. (38) and (42) are not of the same order because the coefficients of $\mathbf{Z}$ are of the order of 10^{-2}. To avoid any discrepancies, Eq. (38) is multiplied by a weight $W = 100$.

Vector $\mathbf{y}$ is given by:

$$\mathbf{y} = \begin{pmatrix} \mathbf{f} - \frac{R}{r_d}I_a\ddot{\boldsymbol{\theta}} \\ W(\mathbf{Z}(\mathbf{f} + I_a(\frac{R}{r_d})^2\ddot{\mathbf{x}}_c) - \mathbf{M}\ddot{\boldsymbol{\alpha}} - \mathbf{g} - \mathbf{c}) \end{pmatrix} \tag{44}$$

and $\mathbf{D}$ is written as:

$$\mathbf{D} = \begin{pmatrix} diag(\mathbf{x}_c) & diag(\dot{\mathbf{x}}_c) & diag(\frac{2}{\pi}\arctan(c_s\dot{\boldsymbol{\theta}})) \\ \mathbf{0}_{3\times 4} & \mathbf{0}_{3\times 4} & W\mathbf{Z}diag(\frac{2}{\pi}\arctan(c_s\dot{\boldsymbol{\theta}})) \end{pmatrix}. \tag{45}$$

Friction parameters are also identified independently for the purpose of comparison with the global identification. In this case, there are only $n_p = 4$ parameters to identify, $\mathbf{v} = \mathbf{f}_s = [f_s(1), f_s(2), f_s(3), f_s(4)]^T$ and:

$$\mathbf{y} = \mathbf{f} - \frac{R}{r_d}I_a\ddot{\boldsymbol{\theta}}, \tag{46}$$

$$\mathbf{D} = diag(\frac{2}{\pi}\arctan(c_s\dot{\boldsymbol{\theta}})). \tag{47}$$

5.2 Identification method

The motor forces $\mathbf{f}$ and motor angular positions $\boldsymbol{\theta}$ as well as the joints orientation angles $\boldsymbol{\alpha}$ are sampled along a specific trajectory to obtain r sampled values. Then, $\mathbf{v}$ can be estimated as the least square solution $\hat{\mathbf{v}}$ of the linear system:

$$\mathbf{W}\mathbf{v} + \rho = \mathbf{Y}, \tag{48}$$

where $\mathbf{W}$ is a $(r \times n_p)$ observation matrix defined by a sampling of the regressor $\mathbf{D}$ defined in (45) or (47), $\mathbf{Y}$ is a sampling of $\mathbf{y}$ defined in (44) or (46), ρ is the vector of residues or vector of errors. The number r of samples must be greater than the number of parameters to identify: $r > n_p$ [39].

The parameter vector $\mathbf{v}$ minimizing the 2-norm of ρ is given by:

$$\mathbf{v} = \mathbf{W}^{+}\mathbf{Y}. \tag{49}$$

The quality of the solution depends on the rank of the condition number of $\mathbf{W}$, that depends on the choice of the trajectory during the identification process. If the measurement noises are independent in $\mathbf{W}$ and $\mathbf{Y}$, the quality of the identification can be evaluated with the covariance matrix $\mathbf{C}_X$:

$$\mathbf{C}_X = \sigma_\rho^2(\mathbf{W}^T\mathbf{W})^{-1}, \tag{50}$$

where $\sigma_\rho^2 = \frac{||\mathbf{Y}-\mathbf{W}\mathbf{v}||^2}{r-N_p}$. The standard deviation of the i-th parameter is $\sigma_i = \sqrt{\mathbf{C}_X(i,i)}$ and the confidence interval is given by $2\sigma_i$. The relative standard deviation $100\frac{\sigma_i}{\mathbf{v}_i}$ evaluates the quality of identification of parameter i

5.2.1 Filtering aspects

The data used for the identification are the measurements of the motor angular positions θ, the input actuation forces $\mathbf{f}$ (assuming that the electrical response of the motors is perfect) and the manipulator configuration α evaluated from the image processing. Cable elongations are deduced from (27), after an initialization in straight position. The derivatives of the measured quantities are calculated by centered numerical differentiation after filtering.

It is essential to filter the measured data to avoid bias arising from noisy discrete measurements [41]. A lowpass Butterworth filter is used to filter the measurements in forward and reverse direction with the Matlab *filtfilt* function. The derivatives of θ are obtained with a central difference algorithm to avoid phase shift. The cutoff frequency of the Butterworth filter is computed with the method explained in [37].

The video frequency used to measure the orientation of the X-joints orientation is $30Hz$ while the frequency of the control law is $500Hz$. To synchronize the data, the motor encoder measurements are resampled with the 'decimate' Matlab procedure to $31.25Hz$, the value closest to $30Hz$. The data from video is also resampled to $31.25Hz$ with a linear interpolation.

5.2.2 Identification trajectory

An excitation trajectory must be designed for the identification in order to improve estimation accuracy [42]. Regarding cable elasticity, the trajectory must be executed with a large exploration of applied forces since cable tensions depend mostly on the latter. Regarding friction, the trajectory must be chosen in order to meet the largest set of possible values of $\mathbf{Z}(\alpha)$. Accordingly, the identification trajectory is defined so that it meets a large set of configurations α and thus requests high forces. Symmetric motions with respect to the straight configuration are considered, knowing that the actuation differs on the right and left sides. The identification trajectory is composed of four successive sequences. Each sequence is composed of the following 6 elementary motions: starting from its straight configuration, the manipulator moves to a desired α^d, moves backward to the opposite configuration $-\alpha^d$, goes back to the straight configuration, moves to $-\alpha^d$, moves backward to α^d and finally goes back to the straight configuration. For the first sequence, all joints move in the same direction and $\alpha^d = [40°, 30°, 20°]^T$. For the second (resp. third, fourth) sequence, the first (resp. second, third) joint moves in the opposite direction to that of the other joints: $\alpha^d = [-40°, 30°, 20°]^T, [40°, -30°, 20°]^T, [40°, 30°, -20°]^T$, respectively. All desired joint configurations are connected with cycloïdal functions. A closed loop control is used to follow the identification trajectory. The identification process being not affected by the performance of the control, the closed loop is simply tuned to produce smooth actuation force variations.

Video recording of the identification trajectory can be found at: `https://uncloud.univ-nantes.fr/index.php/s/8wzgsPi65cxDxG9`.

5.3 Results with linear cable stiffness

The identification of friction is conducted with two different models: the complete model defined by (44) and (45), and the model without cable elasticity defined by (46) and (47). Results are given in Table (1). According to the relative standard deviation, the friction and stiffness coefficients are well identified. The friction parameters are similar whether identified with the elastic cable model or not. The first three friction coefficients are associated with the three cables pulling on the right. It is apparent that $f_s(3) > f_s(2) > f_s(1)$, which is due to pulley friction. Indeed, the number of pulleys met by cables increases with the cable index and so does friction. Since the contribution of $diag(\dot{\mathbf{x}}_\mathbf{c})\mathbf{c}_\mathbf{a}$ in Eq.(42) is limited, the damping coefficients are not well identified as shown by the standard deviation. In fact, a variation of the damping coefficients c_{ai} from 0 to 3000 has a limited impact on the other coefficients, with a variation less than 5%. In the following, a large value is chosen for all damping coefficients in order to damp the elongation in our model: $c_{ai} = 3000, i = 1, ..4$.

	Ident. with (44), (45)	Ident. with (46), (47)
$f_s(1)(N)$	14.42	14.13
relative σ_i	1.68%	2.52%
$f_s(2)(N)$	17.65	17.70
relative σ_i	1.38%	2.02%
$f_s(3)(N)$	18.77	18.97
relative σ_i	1.32%	1.88%
$f_s(4)(N)$	16.18	16.29
relative σ_i	0.88%	1.25%

Stiffness	
$k(1)\ (N.m^{-1})$	10454
relative σ_i	1.28%
$k(2)\ (N.m^{-1})$	9256
relative σ_i	1.37%
$k(3)\ (N.m^{-1})$	8319
relative σ_i	1.60%
$k(4)\ (N.m^{-1})$	5336
relative σ_i	1.85%

Damping	
$c_a(1)\ (N.s.m^{-1})$	805
relative σ_i	30.5%
$c_a(2)\ (N.s.m^{-1})$	333
relative σ_i	68.7%
$c_a(3)\ (N.s.m^{-1})$	-218
relative σ_i	94.3%
$c_a(4)\ (N.s.m^{-1})$	370
relative σ_i	64.3%

Table 1: Identified parameters.

We want to assess the quality and interest of identification. The identification model relies on Eqs. (38), (42). Thus, we verify if these equations are well satisfied with the identified model. We also want to show how the identified model improves results with respect to a model with no friction and no cable elongation.

Eqs. (38) can be rewritten as follows:

$$\mathbf{Z}(\alpha)\mathbf{f} = \mathbf{Z}(\alpha)(diag(\frac{2}{\pi}\arctan(c_s\dot{\theta}))\mathbf{f}_s - I_a(\frac{R}{r_d})^2\ddot{\mathbf{x}}_c) + \mathbf{M}(\alpha)\ddot{\alpha} + \mathbf{c}(\alpha,\dot{\alpha}) + \mathbf{g}(\alpha). \tag{51}$$

Let Γ_m be the torque vector calculated from motor forces: $\Gamma_m = \mathbf{Z}(\alpha)\mathbf{f}$. Let Γ_{rf} (resp. Γ_r) be the torque vector reconstructed with the right-hand side (RHS) of Eq.(51) with friction (resp. with no friction):

$$\Gamma_{rf} = \mathbf{Z}(\alpha)(diag(\frac{2}{\pi}\arctan(c_s\dot{\theta}))\mathbf{f}_s - I_a(\frac{R}{r_d})^2\ddot{\mathbf{x}}_c) + \mathbf{M}(\alpha)\ddot{\alpha} + \mathbf{c}(\alpha,\dot{\alpha}) + \mathbf{g}(\alpha), \tag{52}$$

$$\Gamma_r = \mathbf{Z}(\alpha)(-I_a(\frac{R}{r_d})^2\ddot{\mathbf{x}}_c) + \mathbf{M}(\alpha)\ddot{\alpha} + \mathbf{c}(\alpha,\dot{\alpha}) + \mathbf{g}(\alpha). \tag{53}$$

Figure (4) shows the plots of Γ_m, Γ_{rf} and Γ_r. The goal is to highlight the contribution of the friction terms and to show that these terms must be taken into account. The values of the friction parameters identified with or without the elastic model (e.g., in the first and second column of Table 1) being very close, the corresponding plots in Fig. (4) cannot be distinguished. It is apparent that the friction model improves reconstruction of $\mathbf{Z}(\alpha)\mathbf{f}$. The mean error between the measured values and the values evaluated by the model is $0.18 N.m.rad^{-1}$ when friction is considered but it is $0.55 N.m.rad^{-1}$ without friction. Friction also changes the shape of the curves, which the model does effectively. Some errors remain, in particular at low velocities, for which our model is not efficient. More precise friction models [36] or improved control schemes [7] could be used in future. It can be noticed that antagonistically actuated systems are very sensitive to friction. When changing the orientation of a X-joint, one cable winds up when the other unwinds, and the torques produced by friction via matrix $\mathbf{Z}$ add up.

Cable tension can be computed in two ways. The first one is from the forces using the RHS of Eq. (42). The second one is from the stiffness and cable elongation coefficients using the LHS of Eq. (42). Figure (5) shows the corresponding plots. The same shape is observed, but significant differences exist for high tension values. For a better visualization of this phenomenon, the reconstruction error obtained as the absolute difference between the cable tensions calculated with the RHS and LHS of Eq. (42) is plotted against the applied forces in Fig. (6). The reconstruction error clearly increases with cable tension, which suggests that cable stiffness increases with tension. Accordingly, we propose in next section a new model for the cable elongation, with a stiffness coefficient that varies linearly with tension.

5.4 Cable stiffness depending on tension

Non-linear cable models, as in [43], were also tested, but the identification did not significantly improve the results compared to the linear models. Therefore we developed an ad hoc model to fit the observed measurements. The following

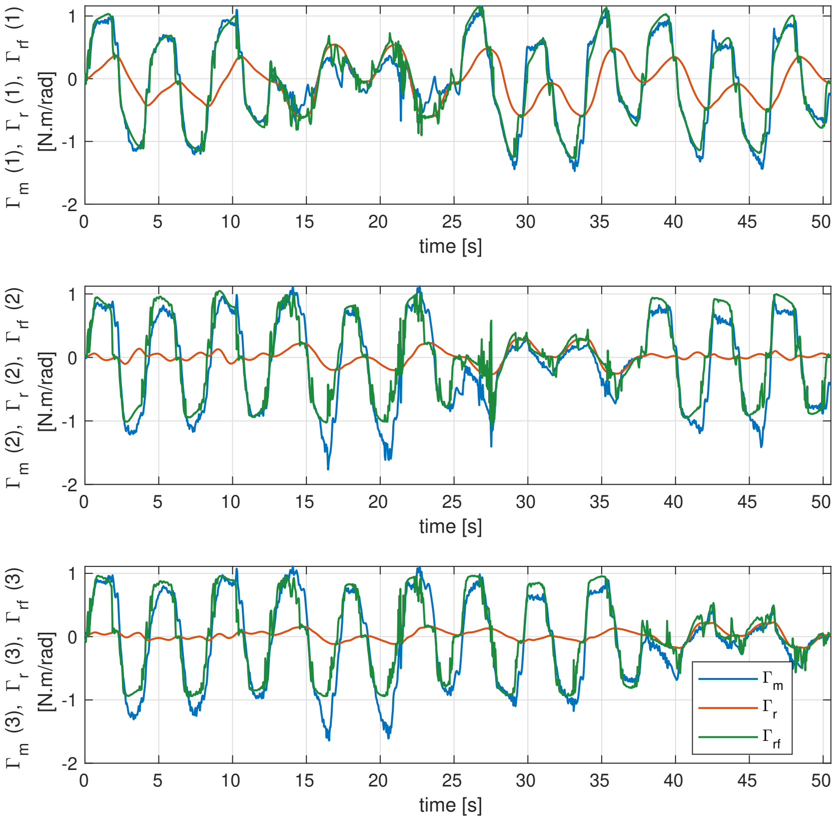

Fig. 4: Time history of torques calculated from the dynamic model with friction (Γ_{rf}, green plot), without friction (Γ_r, red plot) and calculated from motor forces (Γ_m, blue plot).

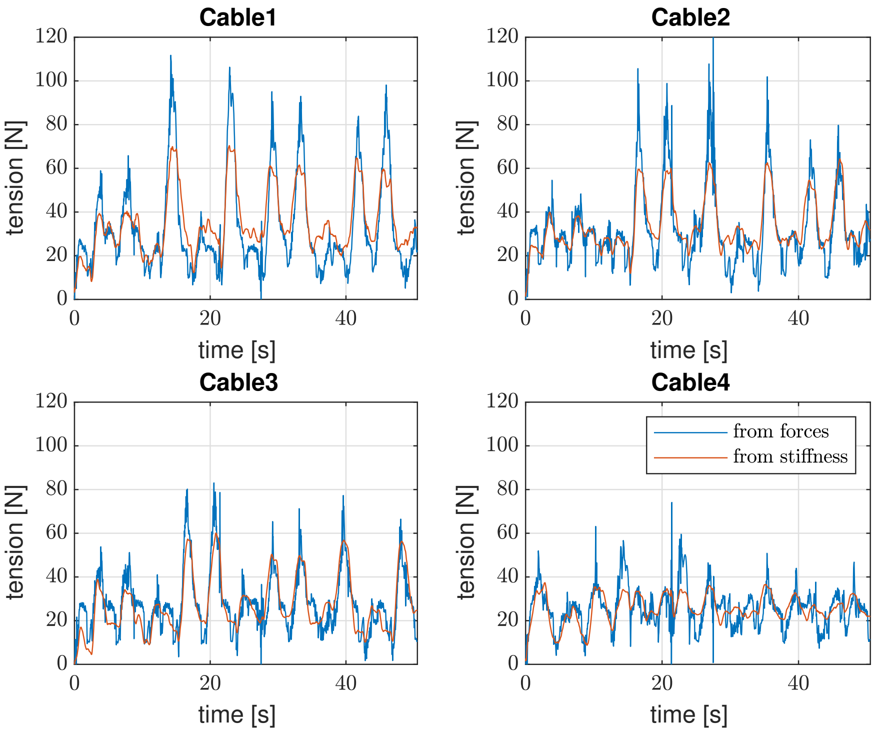

Fig. 5: Cable tension reconstructed from forces and cable stiffness (model with constant stiffness).

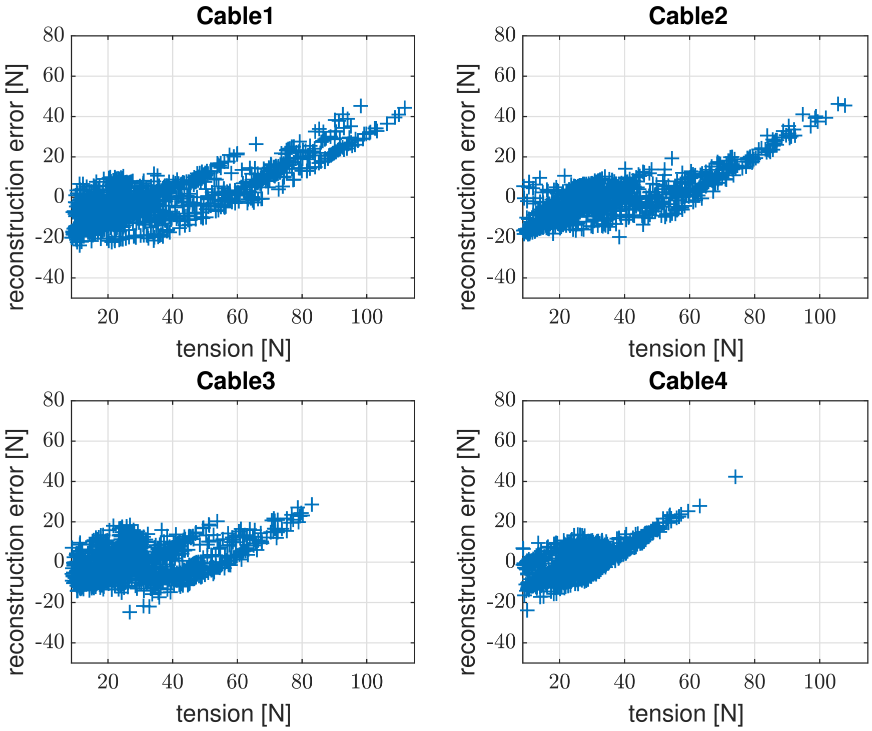

Fig. 6: Reconstruction error as a function of the tension computed from the forces (model with constant stiffness).

new cable stiffness model is proposed:

$$t_{ci} = (k(i) + \lambda(i)t_{ci})x_{ci} + c_a(i)\dot{x}_{ci}, \tag{54}$$

where $\lambda = [\lambda(1), \lambda(2), \lambda(3), \lambda(4)]^T$ is an additional vector to be identified.
Tension in cable i can also be calculated by the i^{th} line of equation (41):

$$t_{ci} = f_i - \frac{2}{\pi}\arctan(c_s\dot{\theta}_i)f_s(i) - \frac{R}{r_d}I_a\ddot{\theta}_i. \tag{55}$$

If Eq.(54) is reported into Eq. (55), we obtain a model that is nonlinear in the parameters $\lambda(i)$ and $f_s(i)$ to identify. In order to build a linear model and since the friction coefficients can be identified separately, the friction parameter values $\mathbf{f_s}$ identified previously can be used. In this case, t_{ci} can be calculated using (55) and the measurements. The identification model is built using (54). It can then be written as (43) where $\mathbf{v}$ if the vector of $n_p = 12$ parameters to identify: $\mathbf{v} = \begin{pmatrix}\mathbf{k} & \lambda & \mathbf{c}_a\end{pmatrix}^T$. Vector $\mathbf{y}$ is defined by:

$$\mathbf{y} = \mathbf{t_c} \tag{56}$$

and $\mathbf{D}$ is:

$$\mathbf{D} = \begin{pmatrix} diag(\mathbf{x}_c) & diag(\mathbf{xt}) & diag(\dot{\mathbf{x}}_c) \end{pmatrix}, \tag{57}$$

where $\mathbf{xt} = [x_{c1}t_{c1}, x_{c2}t_{c2}, x_{c3}t_{c3}, x_{c4}t_{c4}]^T$.

The same method as previously described is used for identification and the identified parameters are given in Table (2). The stiffness parameters are well identified but the damping coefficients are, again, badly identified. The components of the stiffness vector $\mathbf{k}$ are lower than the values obtained in table (1) but they increase with tension since parameters λ are positive.

Stiffness		Stiffness		Damping	
$k(1)\ (N.m^{-1})$	5378	$\lambda(1)\ (m^{-1})$	103.3	$c_a(1)\ (N.s.m^{-1})$	516.8
relative σ	1.6%	relative σ	1.5%	relative σ	14.5%
$k(2)\ (N.m^{-1})$	5364	$\lambda(2)\ (m^{-1})$	88.7	$c_a(2)\ (N.s.m^{-1})$	185.9
relative σ	1.7%	relative σ	2.1%	relative σ	37.8%
$k(3)\ (N.m^{-1})$	6231	$\lambda(3)\ (m^{-1})$	53.2	$c_a(3)\ (N.s.m^{-1})$	-273.3
relative σ	1.7%	relative σ	4.8%	relative σ	22.9%
$k(4)\ (N.m^{-1})$	1908	$\lambda(4)\ (m^{-1})$	120.9	$c_a(4)\ (N.s.m^{-1})$	241.5
relative σ	5.0%	relative σ	2.6%	relative σ	30.7%

Table 2: Identified parameters with the new cable stiffness model (variable stiffness).

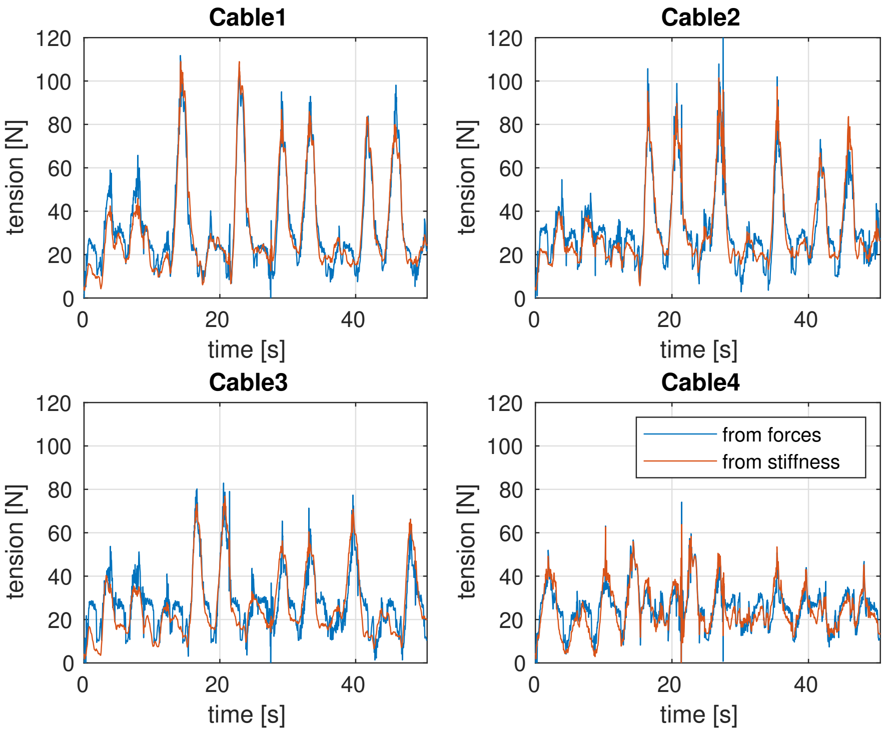

Fig. 7: Cable tension reconstructed from forces and cable stiffness (variable stiffness).

Figure (7) shows the reconstruction of cable tension, calculated in two ways like in Fig. 5. The results are improved as compared to Fig. (5) and tension is well modeled even for high values. The mean error is now $4.75N$, against $6.88N$ with the previous model. The reconstruction error does not increase with the forces.

5.5 Reconstruction of $\hat{\alpha}$ based on cable stiffness model

Now that stiffness is identified, $\hat{\alpha}$ can be evaluated online for control. It can be reconstructed using the elastic model and the measurements of θ. Reconstruction precision is evaluated by comparison with the measurement of α by image processing : α_{IP}. Cable elongation $\mathbf{x}_c$ is estimated with the elastic model. For a short time step Δt, a discrete prediction of the cable elongation by integration of Eq. (54) is:

$$\mathbf{x}_c(t+\Delta t) = \mathbf{x}_c(t) + \frac{\Delta t}{\mathbf{c}_a}(\mathbf{f}(t) - \mathbf{f}_s \frac{2}{\pi} \arctan(c_s \dot{\theta}(t)) - (\mathbf{k} + \lambda \mathbf{f}(t))\mathbf{x}_c(t)). \tag{58}$$

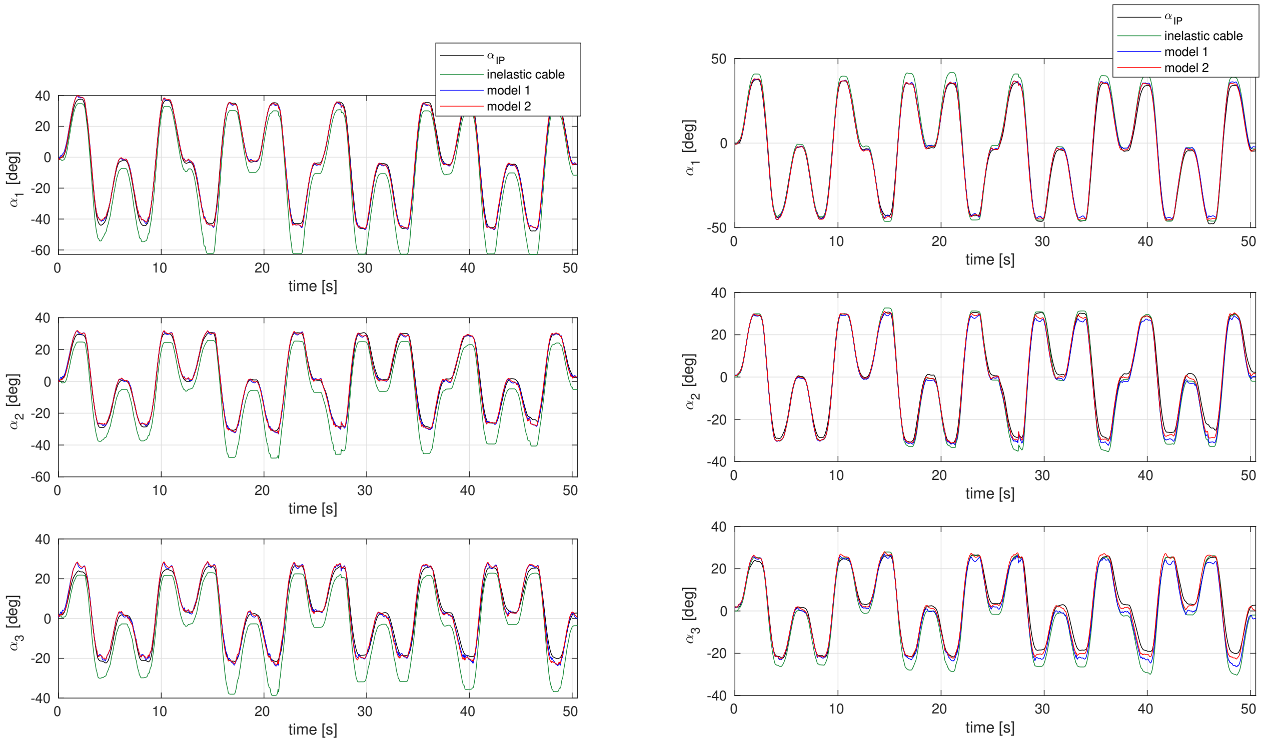

Fig. 8: Left: reconstruction of α using Eq. (33). Right: reconstruction of α using Eq. (35). Green (resp. blue, red) plot corresponds to inelastic cable model (resp. cable model 1, cable model 2). Dark plot shows α measured by image processing

Considering an initial zero elongation, $\mathbf{x}_c$ can be updated at each time step (a sampling period of $2ms$ is used). In the following, three cable models are considered, (i) inelastic cable: $\mathbf{x}_c = 0$, (ii) model 1: cable with constant stiffness ($\lambda = \mathbf{0}$ and $\mathbf{k}$ given in table 1) and (iii) model 2: cable with variable stiffness (λ and $\mathbf{k}$ given in table 2). Then $\hat{\alpha}$ can be computed with only three cable data using Eq. (33) and can also be computed with the four cable data using Eq. (35).

Figure (8) shows the reconstruction $\hat{\alpha}$ and its values obtained via image processing $\alpha_{\mathbf{IP}}$. When $\hat{\alpha}$ is computed from Eq. (33), the mean error without model is $7.87deg$ against $1.67deg$ with the constant stiffness model and $1.51deg$ with the variable stiffness model. When $\hat{\alpha}$ is computed from Eq. (35), the mean error without model is $2.79deg$ against $1.84deg$ with the constant stiffness model and $1.36deg$ with the variable stiffness model. The model of elastic cable gives a better evaluation $\hat{\alpha}$ than the model with no elasticity. The use of four cable data with Eq. (33) is preferable and will be chosen for control purposes.

5.6 Simulator

One of the main objectives of the identification is to have a simulator of the manipulator with a behavior close to the prototype, in order to prepare the experiments in good conditions. Our manipulator is force-controlled, i.e. the inputs are the forces transmitted by the motors to the cables. The role of the simulator is to predict the behavior of the manipulator and, more importantly, the evolution of α and θ, and thus of x_c during motion. The state variables for the simulator are $\alpha, \theta, \dot{\alpha}$ and $\dot{\theta}$. The model is based on (32) and (29). Cable elongation is calculated by (27) and its derivatives. Cable tension is calculated using (54).

A comparison study is conducted between (i) results obtained with the simulator considering no friction and no cable elasticity, (ii) results obtained with the simulator derived from the identification work and (iii) experimental results. The comparison is done with the trajectory and control law used for the identification. The control law will be detailed in section 6 as test1.

Forces applied during experiment are compared with the forces obtained in simulation in Figure (9). Friction and elastic models clearly improve the efficiency of the simulator. Force peaks are better approached. Some of them were not present with the simulator without friction model. Thus, the new simulator is more efficient to prepare our experiments. However, some peaks remain lower with the simulator based on identified parameters, than in experiment. This is due to the identification of friction that is not perfect. Regarding α and θ, plots of their time histories are very close for simulations and experiments. Quantification of the differences is given in table 3.

In the calculation of cable lengths, we have paid particular attention to the effect of the pulleys, whereas their effect was

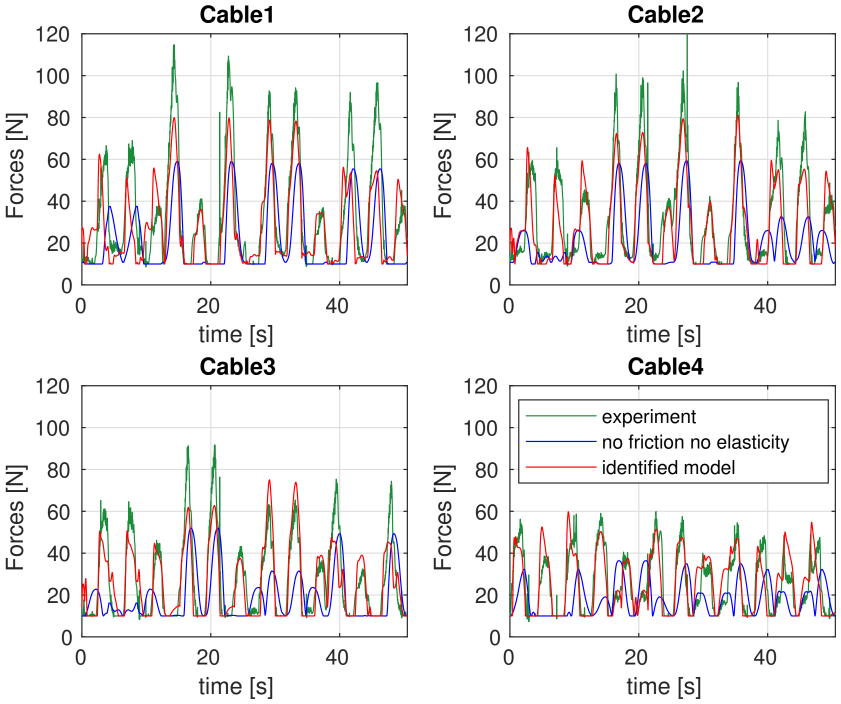

Fig. 9: Comparison of the applied forces in experiment and in simulation.

neglected in [9]. We will now quantify their effects. First of all, we note that pulleys introduce a coupling between the joints: forces exerted by the short cables induce a motion on the lower X-joints. This was not the case when pulleys were neglected, a situation where $\mathbf{Z}_1$ was diagonal.

Three indicators are used here to evaluate the pulley contribution.

The first one is the torques applied on X-joints : we calculate the norm of the difference between the torques calculated with and without pulleys, for a large number of random joint configurations $-\frac{\pi}{2} < \alpha_i < \frac{\pi}{2}$ and applied forces $f_{min} < f_i < f_{max}$. In average, we obtain a difference of 16%.

As a second indicator, the impact on the computation of the orientation of the X-joints α as a function of the position of the encoders θ using (35) is evaluated. A statistical study, for different configurations of the robot $\alpha(t)$ and different displacements of the motor $\theta(t+\Delta t) - \theta(t)$ shows a variation of 13% on average on $\alpha(t+\Delta t) - \alpha(t)$.

The last indicator is evaluated in simulation. The trajectory used for the identification is simulated with two different controls (detailed in next section 6. The two controls consider the friction model and use the pseudoinverse computation of α from θ neglecting cable elasticity. In the first control, we consider the real radius of the pulleys, while in the second control, the radius of the pulleys is neglected ($r = 0mm$). In the two controls, thus, the computation of $\mathbf{Z}$ is not the same, which changes the computation of both the configuration α and the forces f. In robot model used for the simulation, pulleys as well as friction and cable elasticity are taken into account. The first control produces a mean error on the estimation of α of $1.65deg$, versus $2.88deg$ for the second control. Moreover, the mean tracking error (difference between measured α and desired α^d) is $0.12deg$ on α for the first control, versus $0.32deg$ for the second control. Results are summarized in table 3. It is observed that not taking into account pulleys in the control model creates an error that is still greater than not taking into account cable flexibilities and friction in the simulations.

In summary, pulleys have a significant impact on control and must not be neglected.

6 Control

6.1 Computed torque control law

Three control laws are proposed. The first one was used to run the identification trajectory on the prototype. It is now used for the comparison analysis. The objective of the control law is to define the force $\mathbf{f}$ applied by the motor to track a desired trajectory $\alpha^d(t)$ in joint space. A PID controller is used to define the desired joint acceleration $\mathbf{w}(t)$ in closed loop

Control law	simulation with rigid cable model	simulation with identified cable model	experiment
with pulley	e_α = 0.35 deg e = 0.08 deg	e_α = 1.68 deg e = 0.11 deg	e_α = 2.69 deg e = 0.64 deg
without pulley	e_α = 2.00 deg e = 0.21 deg	e_α = 2.88 deg e = 0.26 deg	

Table 3: Mean value for the errors of the estimation $e_\alpha = \alpha - \hat{\alpha}$ and tracking error e in simulations and in experiment. The experiments are only run with a control including pulleys.

as follows:

$$\mathbf{w}(t) = \ddot{\alpha}^d(t) + k_v\dot{\mathbf{e}}(t) + k_p\mathbf{e}(t) + k_i\int_{t'=0}^{t}(\mathbf{e}(t'))dt, \tag{59}$$

where $\mathbf{e} = \alpha^d - \hat{\alpha}$ The gains are: $k_i = \omega^3, k_v = 3\omega$ and $k_p = 3\omega^2$ and we set $\omega = 11$ for all experiments. (59) can be achieved if the controlled forces satisfy the dynamic model in Eq. (32), namely if:

$$\mathbf{M}(\alpha)\mathbf{w}(t) + \mathbf{c}(\alpha,\dot{\alpha}) + \mathbf{g}(\alpha) = \mathbf{Z}(\alpha)\Big(\mathbf{f} - \mathbf{f}_{friction}(\dot{\theta}) + I_a(\frac{R}{r_d})^2\ddot{\mathbf{x}}_c\Big). \tag{60}$$

Now, the following points have to be considered:

- Since the manipulator is over-actuated, infinitely many forces can produce a desired acceleration, but in the same time, cable tensions must remain positive;
- There is no sensor to measure $\mathbf{x_c}$ and α, they have to be reconstructed online from the identification models developed above;
- The online computation of the dynamic model is a bit cumbersome and would become intractable if several X-joints are added. Accordingly, control laws will be designed with a simplified dynamic model.

6.2 Over-actuation and choice of cable tensions

Vector $\mathbf{f}$ appears in Eq. (60) via $\mathbf{Z}(\alpha)\mathbf{f}$ where $\mathbf{Z}$ is a 3×4 matrix and $\mathbf{f}$ is a vector of dimension 4. Let us define:

$$\Gamma^d = \mathbf{M}(\alpha)\mathbf{w}(t) + \mathbf{c}(\alpha,\dot{\alpha}) + \mathbf{g}(\alpha) + \mathbf{Z}(\alpha)(\mathbf{f}_{friction}(\dot{\theta}) - I_a(\frac{R}{r_d})^2\ddot{\mathbf{x}}_c). \tag{61}$$

Then, Eq. (60) is rewritten as $\Gamma^d = \mathbf{Z}(\hat{\alpha})\mathbf{f}$ and, using Eq. (23), as:

$$\Gamma^d = \mathbf{Z}_1(\hat{\alpha})\mathbf{f}_{13} + \mathbf{Z}_2(\hat{\alpha})f_4, \tag{62}$$

where $\mathbf{f}_{13} = [f_1, f_2, f_3]^T$.

Since $\mathbf{Z}_1$ is triangular and invertible, $\mathbf{f}$ can be expressed as a function of f_4 (the force applied on the long cable) as follows:

$$\mathbf{f} = \begin{pmatrix}\mathbf{Z}_1(\hat{\alpha})^{-1}\Gamma^d \\ 0\end{pmatrix} + \begin{pmatrix}-\mathbf{Z}_1(\hat{\alpha})^{-1}\mathbf{Z}_2(\hat{\alpha}) \\ 1\end{pmatrix} f_4. \tag{63}$$

There are thus infinitely many forces $\mathbf{f}$ parametrized by f_4. Two constraints are proposed to select an appropriate solution for control.

The first constraint is to impose a minimal tension $t_{min} > 0$ to avoid slack cables. From Eq. (29), this condition yields:

$$f_i \geq t_{min} + \frac{2}{\pi}\arctan(c_s\dot{\theta}_i)f_s(i) + \frac{R}{r_d}I_a\ddot{\theta}_i. \tag{64}$$

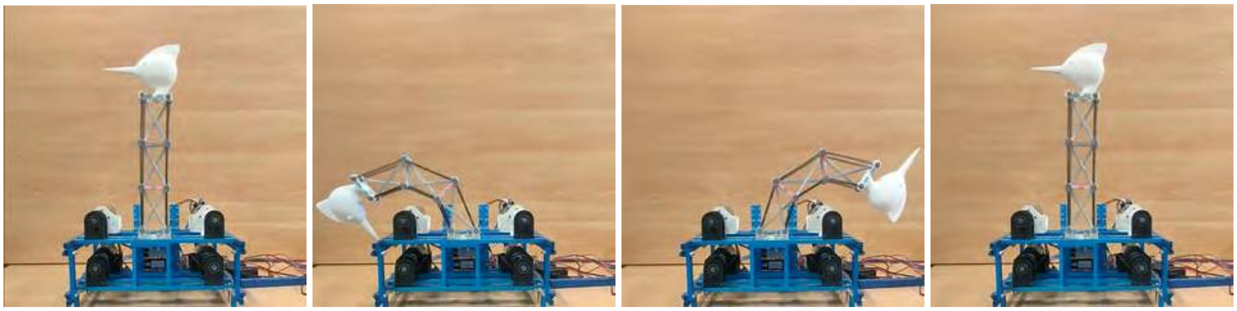

Fig. 10: The main configurations of the trajectory for the control test at $0sec$, $4sec$, $7sec$ and $10sec$, from left to right.

Since our friction model is not accurate at rest, an additional condition is considered for more safety: $f_i \geq f_{min} > 0$. Altogether, each cable force $f_i, 1 \leq i \leq 4$, must satisfy:

$$f_i \geq max(t_{min} + \frac{2}{\pi}\arctan(c_s\dot{\theta}_i)f_s(i) + \frac{R}{r_d}I_a\ddot{\theta}_i, f_{min}). \tag{65}$$

In all experiments, we set $f_{min} = 2N$ and $t_{min} = 8.5N$. These values have been chosen experimentally as the minimal values for which no cable is slack.

The second constraint is to minimize the current consumption of the actuators. Accordingly, the norm of $\mathbf{f}$ is minimized. Due to the antagonist actuation, this constraint induces a minimal force in at least one cable. The applied force is calculated with the following method. Four solutions f_4 to (63) are computed such that $f_i = max(t_{min} + \frac{2}{\pi}\arctan(c_s\dot{\theta}_i)f_s(i) + \frac{R}{r_d}I_a\ddot{\theta}_i, f_{min})$ and the greatest solution is chosen. This choice ensures than all the conditions are satisfied since the components of $-\mathbf{Z}_1^{-1}\mathbf{Z}_2$ are all positive, whatever the value of α. If the resulting force f_i is greater than f_{max}, we take $f_i = f_{max}$. In practice, because the measured values θ_i and $\dot{\theta}_i$ are noisy, they are replaced by the desired values θ_i^d and $\dot{\theta}_i^d$ in (65) to avoid any force discontinuity.

The control law developed for the manipulator at hand can be extended to manipulators with any number N of modules equipped with one long cable on one side and N additional cables on the other side.

6.3 Three control laws

A computed torque control law can be built with Γ^d defined by Eq. (61). To reduce the calculation burden, however, a simplified dynamic model is used. Since the manipulator is light and experienced motions are not very fast, the centrifugal terms as well as the acceleration of the cable elongation can be neglected. Finally, the measurement θ is replaced by the desired value θ^d to avoid variations in the friction term at low velocities:

$$\Gamma^d = \mathbf{M}(\hat{\alpha})\mathbf{w}(t) + \mathbf{g}(\hat{\alpha}) + \mathbf{Z}(\hat{\alpha})(\mathbf{f}_{friction}(\dot{\boldsymbol{\theta}}^{\mathbf{d}})). \tag{66}$$

The orientation angles of the X-joints $\hat{\alpha}$ is calculated with Eq.(35) from the measurements θ. Three different tests are carried out to evaluate the efficiency of the new control, corresponding to the following three control laws:

- test 1: friction and cable elasticity are neglected;
- test 2: friction is taken into account but cable elasticity is neglected;
- test 3: both friction and cable elasticity are taken into account.

7 Control tests analysis

The trajectory used for the control tests involves a motion in the same direction for the three X-joints. This movement seems to be the most interesting to access a large workspace with reasonable forces. Starting from straight configuration, the manipulator moves to $\alpha^d = [50°, 50°, 50°]^T$, goes back to the straight configuration, then moves to $\alpha^d = [-30°, -40°, -50°]^T$, and finally goes back to straight configuration. All desired joint configurations are connected with cycloïdal functions. The four main configurations of the trajectory are shown in Figure (10).

Figure (11) shows the results of test 1 (model with no friction and inelastic cables). Time histories of X-joint orientation angles are plotted for three different values: α^d, which is the desired trajectory, $\hat{\alpha}$, the estimated orientation and α_{IP}, the

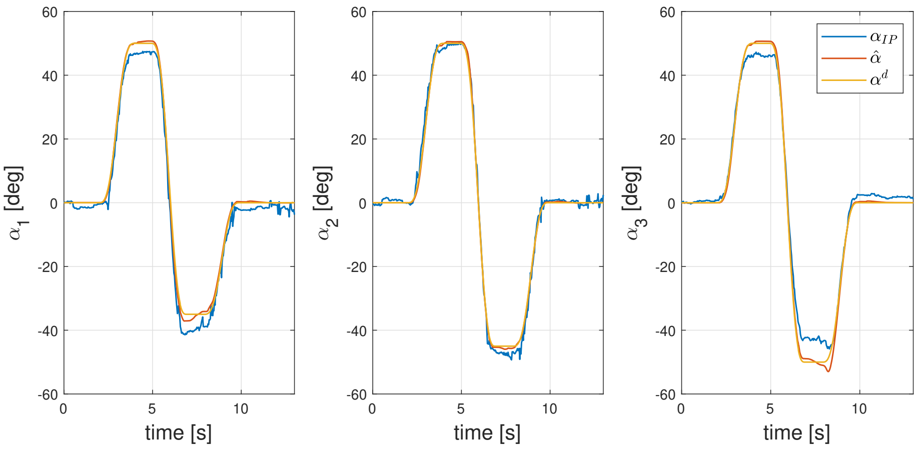

Fig. 11: Time history of joint angles during test 1 (friction and cable elasticity neglected).

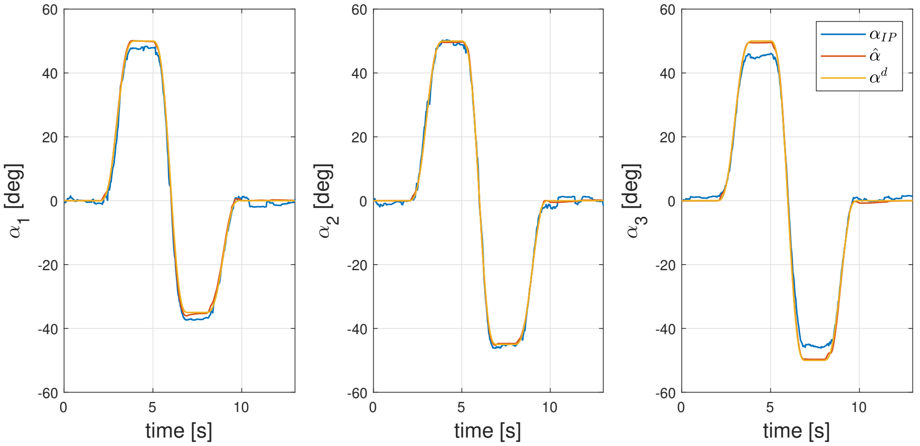

Fig. 12: Time history of joint angles during test 2 (friction is considered but not cable elasticity).

orientation computed offline from video and image processing. The results are fairly good thanks to the computation of $\hat{\alpha}$ with the pseudo-inverse: the mean absolute difference between $\hat{\alpha}$ and α^d is about $0.52deg$. The mean absolute difference between $\hat{\alpha}$ and α_{IP} is about $2.19deg$, which shows that joint angles are not perfectly evaluated. While the tracking error are small, the extreme positions are not well reached since the reconstruction of $\hat{\alpha}$ is not precise enough, especially for joints 1 and 3.

Figure (12) shows the results of test 2 (model with friction and inelastic cables). As expected, results are better than those of the first test. The mean absolute difference between $\hat{\alpha}$ and α^d (resp. between $\hat{\alpha}$ and α_{IP}) is about $0.37deg$ (resp. $1.51deg$). The better prediction of the feed-forward term by the knowledge of the dry friction terms, allows reducing the contribution of the feedback term and reduces tracking errors. In addition, the friction model allows applying lower forces. Less energy is thus required and cable elongation is reduced, which leads to a better estimation $\hat{\alpha}$. The extreme positions are better reached than with the previous model since the estimation $\hat{\alpha}$ is slightly improved, but errors are visible on joints 1 and 3.

Figure (13) shows the results of the last test (model with both friction and cable elasticity). The improvement of the estimation $\hat{\alpha}$ produces a reduction of the mean absolute difference between $\hat{\alpha}$ and α_{IP}, which is now about $1.09deg$. The extreme positions are also better reached than in the other experiments. However, the mean absolute difference between $\hat{\alpha}$ and α^d is about $0.66deg$, which is a bit greater than in the previous experiments. This increase in the tracking errors might be due to the computed control law that resorts to Eq. (66) where cable elasticity is neglected. A control law based on a dynamic model with elastic cables could have been defined. However, such a model would require calculation of the derivatives of the cable elongation, which would add noise.

To finish, we now compare the forces and errors for the three control tests. Figure (14) shows the applied forces during the three experiments. The reference trajectory includes displacement phases and stop phases. In stop phases, the condition

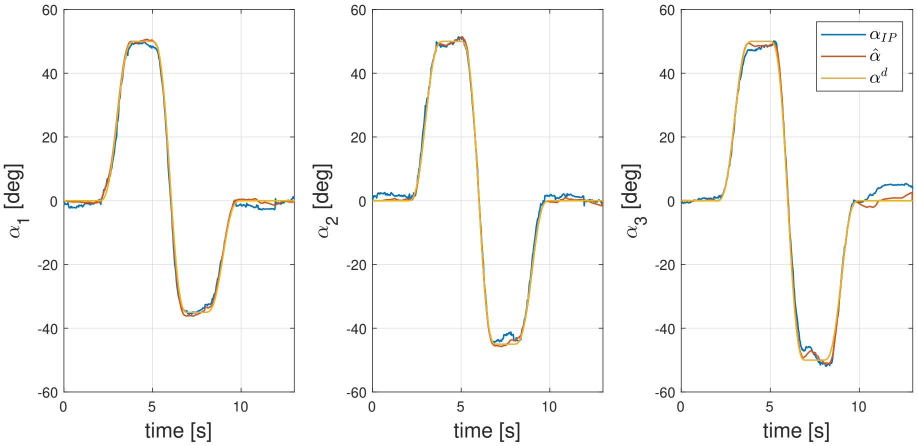

Fig. 13: Time history of joint angles during test 3 (both friction and cable elasticity are considered).

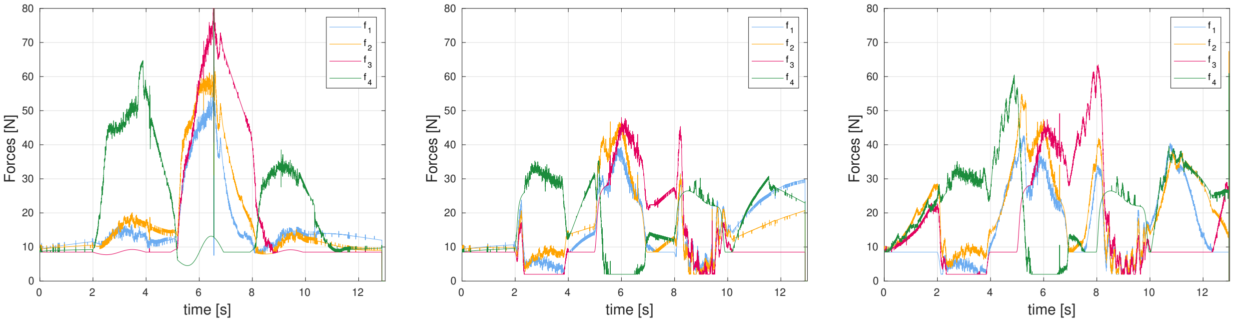

Fig. 14: Applied forces during tests 1, 2 and 3 (from left to right).

on minimum cable tension imposes one of the forces to be $8.5N$ and the other forces to be larger. In the motion phases and for test 1 (no friction, no cable elasticity), the minimum force varies slightly about $8.5N$ depending on the expected motor acceleration. For tests 2 and 3 that take into account the identified friction, we observe that the minimum motor force is $f_{min} = 2N$ since friction tends to tighten cables and the condition on minimum tension is naturally satisfied. This explains the differences observed during the movement phases between control test 1 where the forces are quite high and control tests 2 and 3 where the forces are almost identical and lower. In stop phases, the forces vary mainly because of the integral correction term. In tests 1 and 2, the forces vary gently. For test 3, since the estimation $\hat{\alpha}$ depends on the applied forces, the error detected in the control increases with the forces and the integral term increases. We have tried to remedy this problem by using a PD control. By doing so, similar forces as in test 2 have been produced, but the control has become less efficient and tracking errors have increased.

The differences between the $\hat{\alpha}$ and the values obtained from the video $\boldsymbol{\alpha_{IP}}$ are shown in Figure (15). The mean absolute differences are $2.19deg$, $1.51deg$ and $1.09deg$ for tests 1, 2 and 3, respectively. In tests 1 and 2, the maximal difference is about $8deg$ against $4deg$ for test 3. This shows the efficiency of the elastic model. The mean absolute error is lower in test 2 than in test 1. This can be explained by lower applied forces that produce lower elongation and so lower errors on the estimation $\hat{\alpha}$.

The differences between the $\hat{\alpha}$ and the desired values $\alpha^{\mathbf{d}}$ are shown in Figure (16). The mean absolute error are $0.52deg$, $0.37deg$ and $0.66deg$ for test 1, 2 and 3, respectively. Friction model improves control, with a maximal error twice lower in test 2 than in test 1. The elastic model, however, disrupts control because this model is used only for the estimation $\hat{\alpha}$.

The control law used for test 2 appears as a good compromise: produced forces and control errors are lower than in tests 1 and 3, while the errors between $\hat{\alpha}$ and the value measured by image processing are acceptable.

Video recording of the second test can be found at: `https://uncloud.univ-nantes.fr/index.php/s/x9PPzXPnJHLGWpm`.

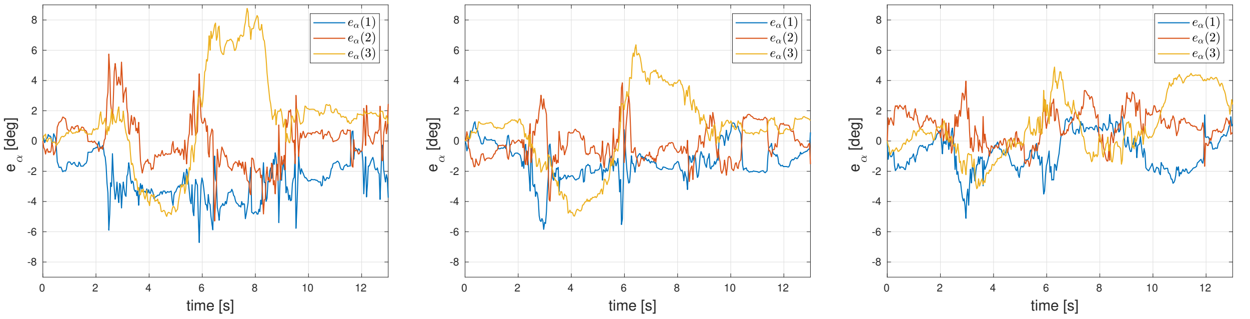

Fig. 15: Error e_α between $\hat{\alpha}$ (computed with pseudo inverse) and α_{IP} (obtained from video) during tests 1, 2 and 3 (from left to right).

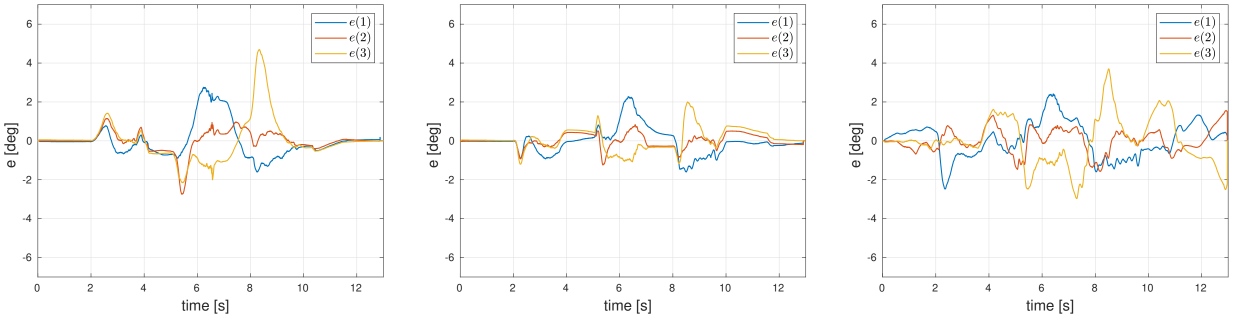

Fig. 16: Error e between $\hat{\alpha}$ (computed with pseudo inverse) and the desired trajectory α^d during tests 1, 2 and 3 (from left to right).

8 Conclusion

The identification and control of a manipulator built with three tensegrity X-joints in series and remotely actuated by cables has been proposed in this paper. Friction and cable elasticity have been identified with excitation trajectories on a test-bed prototype. Friction stems mainly from the geared motors and is increased by the antagonistic actuation. Pulley friction also plays a role. Both friction effects were identified through the proposed friction model. Regarding cable elasticity, elongation plays a role mainly for the estimation of $\hat{\alpha}$ that is not directly measured in our test-bed prototype. The cable stiffness is correctly identified but the damping is not identifiable. A model with constant stiffness did not allow us to reconstruct the tension in the cables in an acceptable way, and we proposed a new model with a variable stiffness that increases with the applied forces and seems better suited to our prototype. This identification phase allowed us to build a suitable simulator to understand our experiments. It also allowed us to elaborate several control laws based on the dynamic model of our system. Modeling friction turned out to be of importance since it allows avoiding slack cables without applying large forces. This allows, in turn, limiting energy consumption and cable elongation.

The methodology developed for the test-bed prototype can be applied to manipulators with any number of X-joints. It could be also used for other applications such as cable-driven continuum robots and for cable-driven parallel robots. It is worth noting that antagonistic actuation, which is always present in our study, increases friction since one motor is always counteracting the action of the others. Taking into account friction in the model allows reducing actuation forces and, in turn, cable elongation. Moreover, antagonistic actuation provides additional equations defined by cable redundancy, which makes it possible to reduce errors caused by cable elongation. This explains why, in our context, friction has more significance than cable elasticity for our control. This would not be the case in different applications, such as in suspended cable-driven parallel robots.

In future work, different trajectories corresponding to the main motion types of a bird neck will be tested. In particular, we will experiment explosive motions corresponding to digging into tree trunks. On the other hand, a prototype with ten X-joints is currently under construction. It will be actuated with four cables to stick on the bird neck architecture. Different cable routing strategies will be compared. Identification and control will be carried out and experiments will be conducted for different typical neck motions.

Acknowledgements

This work was conducted with the financial support of the French National Research Agency (AVINECK Project ANR-16-CE33-0025). The authors acknowledge their membership to the CNRS GDR2088 BIOMIM research network.

References

[1] H. Yuan, L. Zhou, and W. Xu, "A comprehensive static model of cable-driven multi-section continuum robots considering friction effect," *Mechanism and Machine Theory*, vol. 135, pp. 130 – 149, 2019.

[2] R. Ozawa, H. Kobayashi, and K. Hashirii, "Classification, and design of tendon-driven mechanisms," *IEEE Transactions on Robotics*, vol. 30, no. 2, pp. 396–410, 2014.

[3] V. Ramadoss, D. Zlatanov, and M. Zoppi, "Kinematic and workspace analysis of minimally routed cable driven open chains," in *Advances in Mechanism and Machine Science, IFToMM WC 2019* (T. Uhl, ed.), vol. 73, (Cham), pp. 2841–2851, Springer, 2019.

[4] D. L. Bakker, D. Matsuura, Y. Takeda, and J. L. Herder, "Design of an Environmentally Interactive Continuum Manipulator," in *Proceedings of the 14th IFToMM World Congress*, (Tapei, Taiwan), pp. 327–336, 2015.

[5] M. Baril, T. Laliberté, F. Guay, and C. Gosselin, "Static analysis of single-input/multiple-output tendon-driven underactuated mechanisms for robotic hands," in *International Design Engineering Technical Conferences and Computers and Information in Engineering Conference*, vol. 2: 34th Annual Mechanisms and Robotics Conference, Parts A and B, (Quebec, Canada), pp. 155–164, 2010.

[6] Y. Mao and S. K. Agrawal, "Design of a cable-driven arm exoskeleton (CAREX) for neural rehabilitation," *IEEE Transactions on Robotics*, vol. 28, no. 4, pp. 922–931, 2012.

[7] S. Abdelaziz, L. Barbé, P. Renaud, M. de Mathelin, and B. Bayle, "Control of cable-driven manipulators in the presence of friction," *Mechanism and Machine Theory*, vol. 107, pp. 139 – 147, 2017.

[8] C. Bohmer, M. Furet, B. Fasquelle, P. Wenger, D. Chablat, C. Chevallereau, and A. Abourachid, "Combining precision and power to maximize performance: a case study of the woodpecker's neck," in *44ème congrès de la Société de Biomécanique, Poitiers, France*, 2019.

[9] B. Fasquelle, M. Furet, P. Khanna, D. Chablat, C. Chevallereau, and P. Wenger, "A bio-inspired 3-dof light-weight manipulator with tensegrity x-joints," in *IEEE International Conference on Robotics and Automation (ICRA'2020)*, 2020.

[10] C. Böhmer, O. Plateau, R. Cornette, and A. Abourachid, "Correlated evolution of neck length and leg length in birds," *Royal Society Open Science*, vol. 6, May 2019.

[11] F. R. Buckminster, "Tensile-integrity structures," Nov. 13 1962. US Patent 3,063,521.

[12] R. Motro, "Tensegrity systems: the state of the art," *International journal of space structures*, vol. 7, pp. 75–83, June 1992.

[13] R. E. Skelton and M. C. de Oliveira, *Tensegrity systems*, vol. 1. Boston, MA: Springer, 2009.

[14] D. H. Myszka and J. J. Joo, "A study on the structural suitability of tensegrity structures to serve as morphing aircraft wings," vol. 5B: 42nd Mechanisms and Robotics Conference of *International Design Engineering Technical Conferences and Computers and Information in Engineering Conference*, 08 2018.

[15] N. Kim Pham and E. A. Peraza Hernandez, "Design Exploration of a Tensegrity-Based Twisting Wing," vol. 10: 44th Mechanisms and Robotics Conference (MR) of *International Design Engineering Technical Conferences and Computers and Information in Engineering Conference*, 08 2020.

[16] S. M. Levin, "The tensegrity-truss as a model for spine mechanics: biotensegrity," *Journal of mechanics in medicine and biology*, vol. 2, no. 03n04, pp. 375–388, 2002.

[17] M. Arsenault and C. M. Gosselin, "Kinematic, static and dynamic analysis of a planar 2-dof tensegrity mechanism," *Mechanism and Machine Theory*, vol. 41, pp. 1072–1089, September 2006.

[18] C. D. Crane, J. Bayat, V. Vikas, and R. Roberts, "Kinematic analysis of a planar tensegrity mechanism with pre-stressed springs," in *Advances in Robot Kinematics: analysis and design* (L. J. and W. P., eds.), pp. 419–427, Dordrecht, Germany: Springer, 2008.

[19] P. Wenger and D. Chablat, "Kinetostatic analysis and solution classification of a class of planar tensegrity mechanisms," *Robotica*, vol. 37, no. 7, p. 1214–1224, 2019.

[20] K. D. Snelson, "Continuous tension, discontinuous compression structures," Feb. 16 1965. US Patent 3,169,611.

[21] C. Böhmer, J. Prevoteau, O. Duriez, and A. Abourachid, "Gulper, ripper and scrapper: anatomy of the neck in three species of vultures," *Journal of Anatomy*, vol. 236, no. 4, pp. 701–723, 2020.

[22] V. Muralidharan and P. Wenger, "Optimal design and comparative study of two antagonistically actuated tensegrity joints," *Mechanism and Machine Theory*, vol. 159, p. 104249, 2021.

[23] M. Furet and P. Wenger, "Kinetostatic analysis and actuation strategy of a planar tensegrity 2-X manipulator," *Journal of Mechanisms and Robotics*, vol. 11, no. 6. (2019).

[24] R. J. Caverly and J. R. Forbes, “Flexible cable-driven parallel manipulator control: Maintaining positive cable tensions,” *IEEE Transactions on Control Systems Technology*, vol. 26, no. 5, pp. 1874–1883, 2018.

[25] S. Baklouti, E. Courteille, S. Caro, and M. Dkhil, “Dynamic and oscillatory motions of cable-driven parallel robots based on a non-linear cable tension model,” *ASME Journal of Mechanisms and Robotics*, vol. 9, no. 6, pp. 1–14, 2017.

[26] S. Baklouti, E. Courteille, P. Lemoine, and S. Caro, “Vibration reduction of cable-driven parallel robots through elasto-dynamic model-based control,” *Mechanism and Machine Theory*, vol. 139, p. 329–345, 2019.

[27] S. C. Jacobsen, H. Ko, E. K. Iversen, and C. C. Davis, “Control strategies for tendon-driven manipulators,” *IEEE Control Systems Magazine*, vol. 10, no. 2, pp. 23–28, 1990.

[28] H. Kobayashi and R. Ozawa, “Adaptive neural network control of tendon-driven mechanisms with elastic tendons,” *Automatica*, vol. 39, no. 9, pp. 1509 – 1519, 2003.

[29] G. Palli, G. Borghesan, and C. Melchiorri, “Modeling, identification, and control of tendon-based actuation systems,” *IEEE Transactions on Robotics*, vol. 28, no. 2, pp. 277–290, 2012.

[30] S. Bouchard, C. Gosselin, and B. Moore, “On the ability of a cable-driven robot to generate a prescribed set of wrenchess,” *Journal of Mechanisms and Robotics*, vol. 2, no. 1, 2009.

[31] J. Aldrich and R. Skelton, “Time-energy optimal control of hyper-actuated mechanical systems with geometric path constraints,” in *Proc. 4th IEEE Conf. on Decision and Control, December 15, 2005, Seville, Spain*, pp. 8246–8253, IEEE, 2005.

[32] A. Pott, “Influence of pulley kinematics on cable-driven parallel robots,” in *Latest Advances in Robot Kinematics* (J. Lenarcic and M. Husty, eds.), (Dordrecht), pp. 197–204, Springer Netherlands, 2012.

[33] B. Fasquelle, “Cable lengths calculation, modelling and identification of parameters on a manipulator inspired by bird necks,” technical report, LS2N, Université de Nantes ; Ecole Centrale de Nantes (ECN), Feb. 2021.

[34] A. Van Riesen, M. Furet, C. Chevallereau, and P. Wenger, “Dynamic analysis and control of an antagonistically actuated tensegrity mechanism,” in *ROMANSY 22–Robot Design, Dynamics and Control*, pp. 481–490, Springer, 2019.

[35] B. Fasquelle, M. Furet, C. Chevallereau, and P. Wenger, “Dynamic modeling and control of a tensegrity manipulator mimicking a bird neck,” in *Advances in Mechanism and Machine Science, IFToMM WC 2019* (T. Uhl, ed.), vol. 73, (Cham), pp. 2087–2097, Springer, 2019.

[36] W. Kraus, M. Kessler, and A. Pott, “Pulley friction compensation for winch-integrated cable force measurement and verification on a cable-driven parallel robot,” in *2015 IEEE International Conference on Robotics and Automation (ICRA)*, pp. 1627–1632, 2015.

[37] M. T. Pham, M. Gautier, and P. Poignet, “Identification of joint stiffness with bandpass filtering,” in *Proceedings 2001 ICRA. IEEE International Conference on Robotics and Automation (Cat. No. 01CH37164)*, vol. 3, pp. 2867–2872, IEEE, 2001.

[38] M. T. Pham, M. Gautier, and P. Poignet, “Accelerometer based identification of mechanical systems,” in *Proceedings 2002 IEEE International Conference on Robotics and Automation (Cat. No. 02CH37292)*, vol. 4, pp. 4293–4298, IEEE, 2002.

[39] W. Khalil and E. Dombre, *Modeling, identification and control of robots*. Butterworth-Heinemann, 2004.

[40] M. A. Khosravi and H. D. Taghirad, “Dynamic analysis and control of fully-constrained cable robots with elastic cables: variable stiffness formulation,” in *Cable-Driven Parallel Robots*, pp. 161–177, Springer, 2015.

[41] C. Canudas de Wit, B. Siciliano, and G. Bastin, *Theory of Robot Control*. Springer, 1996.

[42] J. Jin and N. Gans, “Parameter identification for industrial robots with a fast and robust trajectory design approach,” *Robotics and Computer-Integrated Manufacturing*, vol. 31, pp. 21 – 29, 2015.

[43] S. Baklouti, E. Courteille, S. Caro, and M. Dkhil, “Dynamic and oscillatory motions of cable-driven parallel robots based on a nonlinear cable tension model,” *Journal of mechanisms and robotics*, vol. 9, no. 6, 2017.